Molecular Simulation Approaches to Proteins Structure and Dynamics and to Ligand Design

Thesis submitted for the degree of
Doctor Philosophiæ
in Structural and Functional Genomics

Candidate:
Marco Berrera

Supervisors:
Prof. Paolo Carloni
Dr. Sergio Pantano

October, 2006

Contents

Chapter 1

Motivations and Summary

Molecular simulations approaches are powerful tools for structural biology and drug discovery. They provide additional and complementary information on structure, dynamics and energetics of biomolecules whose structures have been determined experimentally [1, 2, 3, 4, 5, 6, 7]. In particular, Molecular Dynamics (MD) simulations [8], along with elastic network analysis [9], offer insights into molecular fluctuations, conformational changes and allosteric mechanisms. In addition, molecular simulation can be used to design novel and potent ligands to a specific target (either a protein or DNA) as well as to estimate ligands potency [10, 11]. Attempts at predicting protein structures using bioinformatics and MD are also increasingly successful [12, 13, 14, 15], as well as approaches that use solely simulation tools [16]. The development of new algorithms and the continuously growing computer power currently allow for the simulation of more and more complex biological systems, such as protein aggregates [7, 17, 18, 19, 20] and protein/DNA complexes [21].

In this context, a number of theoretical techniques (namely molecular dynamics simulations, elastic network analysis, electrostatic modeling and binding energy predictions) have here been applied to the study of specific proteins. On the basis of X-ray protein structures, molecular simulations have provided a detailed description of internal motions and interactions, which are not evident from the experimental data and have functional implications.

First, we have used MD to investigate structural features, focusing on the differences between the solid state and the aqueous solution structures. Over 80% of data in the

PDB [22] are X-ray structures, making protein crystallography the major resource in structural biology. Nevertheless, in a few cases, the structural details might be affected by environmental features, such as the presence of small compounds in the buffering solution and/or crystal packing contacts due to the periodic lattice. Here, a comparative MD study has been performed on the Catabolite Activator Protein (CAP), in both the crystal phase and in the aqueous solution. CAP is a bacterial DNA-binding transcription regulator whose activity is controlled by the binding of the intracellular mediator cyclic Adenosine MonoPhosphate (cAMP). CAP is a homodimeric protein and each subunit is formed by a cyclic nucleotide- and a DNA-binding domain. Inspection of the available CAP X-ray structure within the crystal environment [23] suggests that packing contacts do affect the native conformation of the ligand activated protein. Anticipating our results, we have found that indeed the conformation of the protein in solution is different, and that these differences may play a role for CAP biological function.

Next, we have used molecular simulations to target structural flexibility. Conformational fluctuations often play a key role for the protein function and MD simulations can provide information on large-scale concerted motions of proteins [24, 25, 26]. We have addressed this point in the context of the Hyperpolarization-activated Cyclic Nucleotide-modulated (HCN) cation channel. The tetrameric HCN channels are opened by membrane hyperpolarization, while their activation is allosterically modulated by the binding of cAMP in the cytoplasm. The cytoplasmic part of the HCN2 channel, which is responsible for the channel modulation, has been here investigated by MD simulations and elastic network analysis, on the basis of the available X-ray structure [27], to earn new insights into the molecular mechanism triggered by cAMP. We have found that, in the presence of cAMP, the protein undergoes a quaternary structure oscillation, in which each subunit moves as a rigid body. This fluctuation, which is not observed in the absence of cAMP, could facilitate the channel opening transition.

Finally, we have moved our attention to an issue relevant for structure-based drug design. Within a long-standing collaboration with Prof. Cattaneo's lab (SISSA and

Layline Genomics), our group has been interested in the design of mimics of proteins involved in the biochemical pathways that lead to the Alzheimer's disease. Here, on the basis of structural information [28], we have designed a peptide that could specifically target trkA, the high affinity receptor of the Nerve Growth Factor (NGF), which is a protein that plays a critical role for the development, survival and maintenance of neurons in the vertebrate nervous system and activates signaling pathways related to neuroprotection. The results of this research will be tested at the Prof. Cattaneo's Lab in order to validate the theoretical findings and assess the potency and the effects of such a ligand.

Chapter 2

Introduction

As mentioned in chapter 1, in this thesis we have used MD simulations and other computational tools to investigate structure and dynamics of proteins and to design peptide mimics. Hereafter, we introduce the specific systems we have been focusing on.

2.1 Catabolite Activator Protein

2.1.1 Biological context

The Catabolite Activator Protein (CAP), also known as the cyclic Adenosine MonoPhosphate (cAMP) Receptor Protein (CRP), is a bacterial activator of the transcription of several operons, including those that code for enzymes involved in the metabolism of sugars like lactose, maltose and arabinose, following the binding of the intracellular mediator cAMP [29, 30, 31, 32, 33]. As glucose level drops, the cell-surface enzyme adenylyl cyclase is activated and converts ATP into cAMP molecules, which is released through the cell. Because of its role in delivering messages from the primary glucose sensor (adenylyl cyclase) to the synthetic machinery, cAMP is often known as a second messenger. When cAMP binds to CAP, it changes the conformation of the protein [34, 31, 32], which thus binds to a specific DNA sequence [35] located next to the genes that are activated. Therefore, the cAMP binding to the protein ultimately results in transcription activation [36, 31, 37].

The selective DNA binding occurs at micromolar concentrations of cAMP and is inhibited at higher ligand concentrations, although the nonselective DNA binding is

not as greatly inhibited [38, 39, 35, 40], suggesting that CAP in the presence of low cAMP concentrations is the active form [41, 35]. This biphasic behavior is due to the presence of two cAMP binding sites for each protein subunit: the primary binding site has high affinity for cAMP and is responsible for the protein activation; the secondary binding site has lower ligand affinity and is responsible for the CAP features in case of high ligand concentration [35]. Because of the different ligand affinity of the two binding sites, the primary sites are preferentially ligand bound before the secondary sites [42].

2.1.2 Structure

The structural basis of the allosteric mechanism activated by cAMP binding to CAP before its interaction with DNA and a model of the DNA bending triggered by the binding of the activated protein have been described on the basis of the X-ray structures of the cAMP-bound CAP from *Escherichia coli* in the DNA-free and DNA-bound states [43, 44, 41, 23] and of the related protein CO-sensing transcription regulator from *Rhodospirillum rubrum* [45], which controls the activation of the transcription of genes involved in the oxidative metabolism of CO.

CAP is a homodimer of 22,500 molecular weight and the two subunits (namely A and B, 209 amino acids each) are formed by two domains each: the N-terminal Cyclic Nucleotide Binding Domain (CNBD, residues 1-137) and the C-terminal DNA-Binding Domain (DBD, residues 138-209). The hinge interdomain region includes residues located close to the homodimeric symmetry axis (residues 133-142).

The DNA-bound and DNA-free structures differ for the DBDs orientation: in the first structure the DBDs are symmetrically arranged and are both packed against their CNBDs (*closed* conformation); DNA is bent by $\sim 90^{\circ}$ [41, 43, 44]. In the latter, one domain is still in the *closed* conformation (A subunit) whilst the other (B subunit) is separated from its corresponding CNBD by a cleft (*open* conformation) [23].

2.1.3 cAMP binding

The CNBD includes an eight-stranded β-roll, which is flanked by the A-helix at its N-term, and by the B- and C-helices at its C-term. cAMP binds in its *anti*-conformation to the so called primary binding sites, which is located within the β-roll and is lined by the C-helices of both subunits (Fig.1a). In fact, the CNBD is responsible for the protein dimerization. cAMP forms H-bonds with the CAP side chains of residues Glu-72, Arg-82, Ser-83, Thr-127 and Ser-128; additional H-bonds are formed with the protein backbone of residues Gly-71 and Ser-83.

A comparative theoretical study has shown that the CNBD is a signaling module that is found in different proteins with conserved structure and function [46]. Details into the structural mechanism activated by cAMP in the CNBDs of the Protein Kinase A (PKA) regulatory subunit and of the HCN2 ion channel has been previously obtained by performing molecular simulation studies, which showed that a change in structural and dynamic features of the secondary structure elements lining the binding site is driven by the ligand [47, 48]. In CAP, the cAMP binding to the CNBDs triggers a reorientation of the $\beta 4/\beta 5$ loops and of the C-helices, which allosterically leads to a change in the hinges and, consequently, to a repositioning of the DBDs [49, 50, 51, 52, 53, 54, 55, 23, 45, 56, 57, 46, 58].

The low-affinity secondary binding sites are formed by residues from both domains of the same subunit and from the hinge region of the opposite chain [44].

2.1.4 DNA binding

Each DBD includes a helix-turn-helix motif (E- and F-helices) involved in the specific recognition of DNA, whose consensus sequence is 5'-AAATGTGATCT-3' [59]. As a consequence of the complexation, a kink in the DNA occurs between nucleotide base pairs 5'-TG-3' (bases 6 and 7 of the above consensus sequence) on both sides of the dyad axis, as is observed in the DNA-bound CAP X-ray structure, in which the DNA is bent by nearly 90° [43, 60, 61, 62, 63, 64]. This sequence has been shown to favor DNA flexibility and bending also in other systems [33, 65].

The DNA binding induces a change in the conformation of CAP, in particular affecting regions of the protein which are involved in interactions with other members of the transcription machinery [66,67,68,69,70], even away from the protein-DNA contact region, as the B-helix [70]. This suggests that DNA binding may play a role in the modulation of the protein-protein interactions of CAP. The regulation of transcription factors activity by DNA-induced conformational changes has been documented in a number of eukaryotic systems [71].

Following the CAP binding to DNA, RNA polymerase is recruited for transcription activation. CAP contains activating regions that have been proposed to participate in direct protein-protein interactions with RNA polymerase and/or other basal transcription factors. Specifically, protein-protein interactions with RNA polymerase were identified by mutagenesis experiments in the surface loop formed by residues 156-164 (residues Ala-156, Thr-158, His-159, and Gly-162) [66, 67] and in residues His-19, His-21, Glu-96 and Lys-101 [68].

2.1.5 Aims

The structure of the cAMP-activated form of CAP in aqueous solution and the effect of crystal packing on the protein conformation are investigated by molecular dynamics simulations. The relevance of the solution structural model for CAP biological function is investigated.

2.2 Ion channels

2.2.1 Biological context

The regulation of ion concentration and permeation is of crucial importance for a variety of cellular functions, such as nervous signal transmission and osmotic regulation. These functions are controlled by ion channels, which are proteins inserted in the membrane lipid bilayer. They form aqueous pores through the cell membrane and provide a feasible path for ion exchanges. By allowing ions to cross the hydrophobic barrier of the core membrane, they control the cellular exchange of ionized particles. Several ionic channels are known and they differ in functional, gating and selectivity properties [72].

In resting conditions, the internal side of a cell has a lower electrostatic potential than the external side. When ions flow through the channels, they produce an electric current and a change of the membrane potential. The conducting state of the channel may be regulated by different factors that open and close the channel mouth, regulating the ion current [72]. The gating mechanisms can be based on physical factors, like the transmembrane potential difference in voltage-gated channels [73], which are important for the transduction and the propagation of the electric signal in the human and animal nervous system [74, 75], or the pressure-induced structural changes in mechanosensitive channels [76]. In other classes of channels, chemical factors are also regulators of the channel gating, as the presence of ligand molecules in, for example, the cyclic nucleotide activated channels [77, 78], or pH variations in, for example, the KcsA potassium channel [79].

An important property of the open channel is the selective permeability, which is the ability to allow only to a restricted class of ions to flow through the channel pore in large amount [80]. Channels may discriminate between ions with different valence and charge, as in chloride channels [81], or between divalent cations over monovalent cations, as in calcium channels [72].

Many human and animal diseases are associated to defects in ion channels function, the majority of them arising from mutations in the genes that encode the channel proteins [82, 83, 84, 85, 86, 87, 88]. Large effort is still necessary to connect these mutations

to the structural and functional changes that cause the disorder.

2.2.2 HCN Channels

The Hyperpolarization-activated Cyclic Nucleotide-modulated (HCN) cation channels belong to the voltage-gated channels superfamily. They are opened by membrane hyperpolarization, while the binding of cyclic Adenosine MonoPhosphate (cAMP) modulates their activity. The HCN channels family includes four members (HCN1–4) that are expressed in cardiac and neuronal cells of vertebrates. [89,90,91,92,93,94,95,96,97, 98,99,100,101,102,103,104]. HCN channels control fundamental biological events such as heart beat and neuronal rhythmic activity, providing the biophysical mechanism for the pacemaker in these cells [105, 106, 107, 108]. Although these channels clearly contribute to the determination of the resting potential of the cells in which they are expressed, their role in dynamic signaling events is less well understood.

Hyperpolarization-activated cation currents (Ih) have puzzled physiologists since their initial discovery 30 years ago [109]. Unlike most voltage-gated currents, Ih are activated by transmembrane hyperpolarization, i.e. by potentials more negative than the resting potential: this property earned them the designation of If for 'funny' [110] or Iq for 'queer' [108]. Ih current plays a role in the generation of spontaneous pacemaker activity both in the heart [105] and in the central nervous system [106]. The Ih current that flows through HCN channels [111] is carried by a mixture of Na+ and K+ ions [112,113] and is blocked by Cs+ ions in a voltage-dependent way [114].

The recent identification of a family of four mammalian genes that encode the hyperpolarization-activated cation channels, HCN1-4 [99], gave the opportunity to address the physiological function of Ih at the molecular level. All four isoforms have been expressed in heterologous cells and form tetrameric, hyperpolarization-activated cation channels that are directly modulated by cAMP. However, the four HCN isoforms give rise to channels that differ in their kinetics, steady-state voltage dependence and potency of modulation by cAMP [115]. Given the diversity of native Ih in different cell types, a key goal is to relate the cellular heterogeneity to the molecular composition of the channel. This is complicated by the fact that native pacemaker currents

exhibit greater diversity, for example with regard to voltage dependence, than the expressed isoforms [116]. In addition, on the basis of the amino acid sequence, these four mammalian genes were shown to be members of the voltage-gated channels superfamily [97].

Related HCN genes have been also characterized in invertebrate organisms and have been cloned from the sea urchin *Strongylocentrotus purpuratus* sperm (spHCN) [117], from the silkmoth insect *Heliothis virescens* antennae (hvHCN) [118], from the *Drosophila melanogaster* antennae and eyes (DmHCN) [119] and from the olfactory receptor neurons of the bee *Apis mellifera* (AmHCN) [120]. These channels show a high sequence homology to the vertebrate counterparts in functionally relevant regions like the membrane spanning domains, in particular the S4-voltage sensor and the pore region, and the cyclic-nucleotide binding region. The most pronounced differences between the channel sequences are found in the length of their N-terminal regions [120].

2.2.3 Structure

HCN channels are tetrameric and each monomer comprises three conserved domains (Fig.2.1). The first is the transmembrane domain, which is formed by six transmembrane helices including a positively charged S4 voltage sensor, similar to the voltage sensor of the depolarization-activated channels; this domain is responsible for the ion selectivity and the channel gating. It is connected to the C-linker domain in the cytoplasm, which in turn is linked to the Cyclic Nucleotide Binding Domain (CNBD). These three domains are highly conserved with 80-90% sequence identity [100]. However, the genes products diverge in their N- and C-terminal cytoplasmic regions.

In a seminal article [27], Zagotta and co-workers have determined the X-ray structure of C-linker and CNBD of HCN2 from mouse in complex with four equivalents of cAMP. The C-linker is composed by six α-helices (A'–F'), establishing a large amount of intersubunit contacts and coupling the channel gating transmembrane part to the CNBD [27, 121]. The CNBD includes four α-helices (A, P, B, C) and an eight-stranded β-roll, arranged with the same fold observed in the CNBD of other proteins [43, 122, 123, 124, 125, 126, 23, 127, 41]. cAMP binds in its *anti*-conformation to a

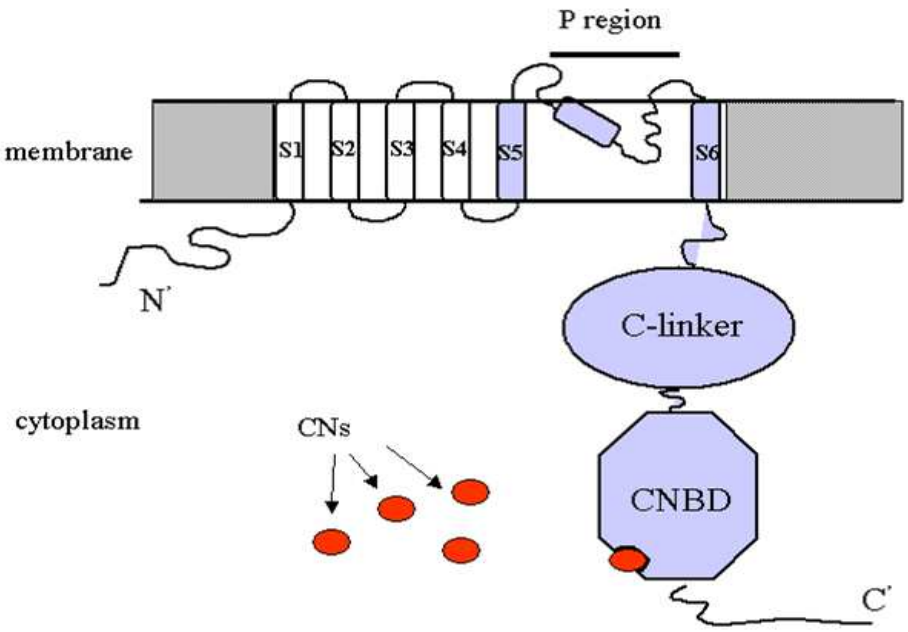

Figure 2.1: Diagram of an HCN channel subunit. The intramembrane part includes 6 transmembrane helices and is followed by the C-linker and the CNBD in the intracellular compartment.

highly conserved region lined by the β-roll, P- and C-helices. Its phosphate and OH groups H-bond to a bunch of residues from position 581 to 593, which includes the P-helix and the following loop. These residues constitute the signature motif of the CNBDs, called the phosphate-binding cassette [46]. The purinic group of the ligand forms contacts with the β-strands 4 and 5 (Val-564, Met-572, and Leu-574) and the C-helix (Arg-632 and Ile-636) [27].

2.2.4 cAMP Modulation

In all four HCN isoforms, the 120-amino acid length CNBD mediates the channel response to the intracellular cAMP. This domain is homologous to similar regions in other cyclic nucleotide binding proteins, including the cAMP- and cGMP-dependent protein kinases, the bacterial Catabolite Activating Protein (CAP) and the Cyclic Nucleotide-Gated (CNG) ion channels of olfactory neurons and photoreceptors [46].

HCN2 is the best characterized member of the family. In this channel, the CNBD inhibits channel activity by a mechanism which depends on the C-linker/CNBD interactions: binding of cAMP relieves this inhibition and shifts by ∼+17 mV the voltage dependence to less negative values [103, 104]. In fact, the deletion of the CNBD mimics the effect of cAMP by shifting the voltage dependence of HCN2 gating to more positive voltages by an amount similar to the maximal shift due to saturating concentrations of cAMP [103, 104]. This indicates that cAMP enhances gating by relieving the inhibitory effect of the CNBD, which shifts the gating in the absence of cAMP to more negative potentials. Differences in the voltage dependence of gating and in the potency of cAMP modulation between HCN1 and HCN2 were shown to result from differences in the extent of inhibition produced by the CNBD, HCN2 having a much greater inhibition than HCN1 [103, 104].

2.2.5 Aims

The structural and dynamic features of the cytoplasmic part of the HCN2 channel in the ligand bound and free states are investigated by molecular dynamics and elastic network analysis, to gain insights into the allosteric mechanism of cAMP modulation of the HCN2 channel.

2.3 Nerve Growth Factor

2.3.1 Neurotrophins

Neurotrophins constitute a family of structurally related proteins, which promote and regulate the survival of neurons in the vertebrate nervous system [128, 129, 130]. This family includes the Nerve Growth Factor (NGF), the Brain-Derived Neurotrophic Factor (BDNF), the Neurotrophin-3 (NT-3) and the Neurotrophin-4/5 (NT-4/5) [131]. They bind with similar affinity to the receptor $p75^{NTR}$, a member of the Tumor Necrosis Factor (TNF) receptor superfamily, and selectively to the members of the receptor tyrosine kinase (trk) family, namely trkA, trkB and trkC, which are involved in the activation of different intracellular signal transduction cascades [132, 133, 134, 135]. Specifically, NGF binds with the highest affinity to trkA [136, 137, 138], which mediates the survival-promoting and neurite-growth-promoting effects of NGF during development [139, 140, 141, 142] (Fig.2.2a).

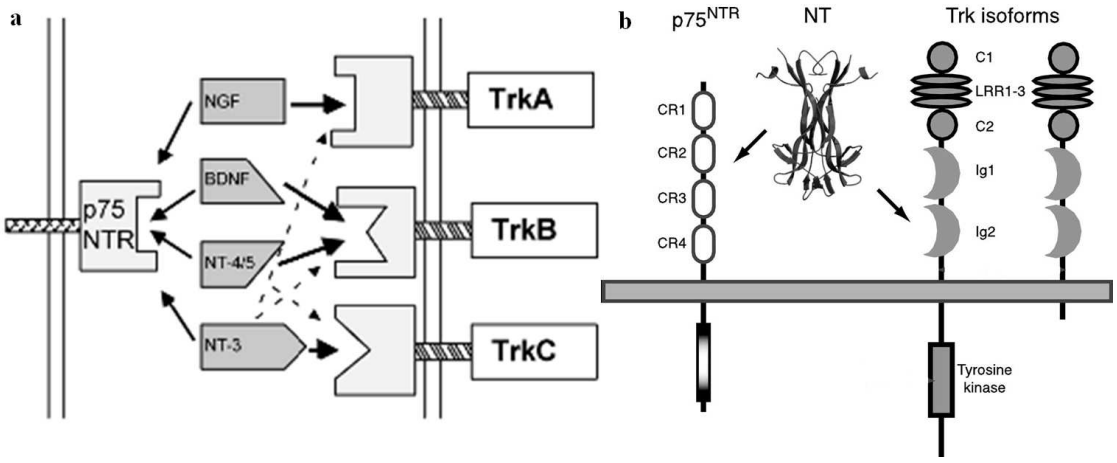

Figure 2.2: (a) Neurotrophins bind to two classes of receptors: the low affinity receptor $p75^{NTR}$ and specifically the members of the trk receptors family. (b) Diagram of the receptors subdomains.

2.3.2 Biological context

The Nerve Growth Factor (NGF) is the most studied and the first identified member of the neurotrophins protein family [139]. NGF was initially found to be an essential factor in the survival of sympathetic and embryonic sensory nerve cells [143], but its

frame of activity was soon extended to many other functions. It is now very well established that NGF plays a central role in the development, survival and repair of peripheral and central nervous tissues of both embryos and adults [144]. In addition, it has been endowed with roles in the immune and endocrine systems, autoimmune disease and tissue inflammation [145].

The role of NGF *in vivo* has been defined to be trophic, differentiative and tropic [146]: NGF exploits its trophic effect on sensory and sympathetic cells being necessary for their survival; its differentiative effect is due to its role in the differentiation of the same cells to mature nerve cells; finally, the tropic effect of NGF consists in its ability to guide the growing axons or collaterals along its own concentration gradient.

An important feature of NGF is the retrograde transport: this neurotrophin, in fact, was shown to be retrogradely transported within neurons *in vivo*, under physiological conditions, allowing the communication of the body cell with the nerve terminal [147, 148]. The retrograde transport is a composite mechanism, involving a series of complex events, like the release of the neurotrophin by the post-synaptic target cell, followed by receptor binding on the nerve terminal pre-synaptic membrane. Subsequently, the protein is internalized, targeted for transport and propelled along the axon toward the cell body [148].

2.3.3 Structure

NGF is a dimeric protein and the dimer is held together by non-covalent interactions [149]. Its 3D structure has been determined by X-ray crystallography, revealing a compact β-structure protein [150, 28]. Three intrachain disulfide bridges form the so called cysteine knot motif. The central core of the protein, formed by the facing β-strands of the two monomers, gives rise to an extensive subunit interface with a largely hydrophobic character, primarily because of aromatic residues. Three β-hairpin loops in the structure of each monomer are composed by most part of the variable residues in different species, while the compact core is conserved.

2.3.4 The NGF receptors

The response of neurons to NGF is governed by two types of cell surface receptors: the receptor tyrosine kinase $p140^{trk}$, which is referred to as trkA [151], and $p75^{NTR}$, which is a member of the Tumor Necrosis Factor (TNF) receptor superfamily (Fig.2.2a). TrkA activation is predominantly followed by survival signaling. On the contrary, the $p75^{NTR}$ receptor, as other members of the TNF superfamily, was demonstrated to modulate apoptotic responses.

The dimerization of the trk receptors upon binding to neurotrophin leads to trans-autophosphorylation and to the activation of intracellular signaling cascades [152]. Signaling modules, such as the RAS/mitogen-activated protein (MAP) kinase cascade and the phosphatidylinositol-3 (PI-3)-kinase/Akt pathway, have been identified as downstream cellular events induced by trkA activation. When $p75^{NTR}$ and trkA are expressed in the same cell, however, survival signaling dominates [151].

Historically, $p75^{NTR}$ was the first receptor of NGF to be identified [153], but a lack of readily identifiable signal transduction modules within its cytoplasmic sequence led to the assumption that the function of $p75^{NTR}$ was primarily to augment trkA signaling [154, 151]. Actually, pro-NGF, which is released as a soluble proneurotrophin and is processed to a mature neurotrophin, is a high affinity proapoptotic ligand for $p75^{NTR}$ [155]. The activation of $p75^{NTR}$ can initiate apoptosis when this receptor is expressed independently of trk. Thus, $p75^{NTR}$ plays diametrically opposite roles in promoting death and augmenting survival [156, 151].

2.3.5 NGF / trkA interaction

The extracellular subdomains of trkA are Cys-rich 1 (d1), Leu-rich motif (d2), Cys-rich 2 (d3), IgGL1 (d4) and IgGL2 (d5), where IgGL refers to the immunoglobulin-like C2 folding motif [148] (Fig.2.2b).

The structural determinants of NGF binding to the fifth extracellular domain of human trkA (trkA-d5) have been provided by the X-ray structure of the complex [28] (Fig.2.2b). This study confirmed an extended surface of interaction of this domain with NGF. The NGF/trkA-d5 interface involves two patches: one comprises residues of NGF

core region and loops of the C-term@trkA-d5, the other includes the N-term@NGF and the 'ABED' β-sheet@trkA-d5 [157, 28]. The latter is known to determine the affinity and specificity of the NGF binding to trkA, as indicated by experimental data [158, 159, 160, 161, 162, 163, 164, 141] and further suggested by Molecular Dynamics calculations [165]. Although only the fifth extracellular domain (d5) is present in the structure, the contribution of the other subdomains to the binding cannot be excluded.

The structure of the mouse NGF alone [166] and that of the human NGF in complex with trkA-d5 [28] display few differences. Apart from unconserved residues, the most striking difference is at the N-terminus. While this segment is disordered in the unbound structures [162, 166], it assumes a helical conformation in the NGF/trkA-d5 complex, forming an important part of the binding interface [28].

2.3.6 Therapeutic applications

Because of their crucial role for nervous system development, neurotrophins may reduce neuronal degeneration in neurodegenerative diseases, such as Alzheimer's [167, 168, 169, 170, 171, 172, 173, 174]. However, the therapeutic efficiency of NGF has been greatly limited by delivery problems and severe side effects [175, 176, 177]. A major obstacle to the neurotrophin-based therapies is that significant protein concentrations must be achieved in the target region to really counteract disease progression and, simultaneously, this delivery must be hampered in other regions to prevent side-effects [175, 176, 177].

A promising strategy involves the use of peptide mimics, i.e. molecules with either agonist or competitive antagonist effect that retain the most essential elements of the neurotrophic action, which may be useful in the treatment of several neurodegenerative diseases and nerve injuries [178, 179, 180, 181]. For NGF, such peptides have been shown to exhibit neurotrophic effects by binding to trkA [182, 183, 184, 185, 186, 187, 188].

2.3.7 Aims

To identify peptide mimics of the neurotrophin NGF with high affinity and specificity for trkA, several computational tools are first used to identify the residues of the N-

terminal fragment of NGF forming significant interactions with the receptor in the NGF/trkA-d5 complex; subsequently, the stability of the adduct is investigated by molecular simulations approaches.

Chapter 3

Methods

We introduce here basic concepts of the techniques used in this thesis, namely molecular dynamics simulations [8], elastic network analysis [9], electrostatics calculations [189] and hot spot binding energy prediction [190, 191]. The specific features of each of the studied systems are reported in the *Computational Details* section of the corresponding chapters.

3.1 Molecular dynamics

The dynamics of proteins cannot be simulated quantum-mechanically due to their large size. We can predict the evolution of such complex systems using Molecular Dynamics (MD) simulations [8]. MD is based on the following assumptions: (i) the nuclei can be treated as classical particles; (ii) the Born-Oppenheimer approximation holds; (iii) the electronic degrees of freedom can be integrated out. Under these greatly simplifying assumptions, the dynamics of the system can be described by the Newton second law:

$$m_i \frac{d^2\vec{r}_i}{dt^2} = -\nabla_{\vec{r}_i} E_{tot}(\vec{r}_1, ..., \vec{r}_N)$$

where $\vec{r}_i$ is the position of the i^{th} atom and E_{tot} is the total energy of the system of N particles. Thus, if one knows the initial structure (by experiments or by computer modeling) and provides a velocity distribution consistent with the temperature simulated, one can provides the time-evolution of the system. MD average values of several properties can be evaluated from the resulting trajectory.

In the followings, the form of E_{tot} used for proteins and some details of MD algorithms are given.

3.1.1 Force Field

The potential energy function here used (E_{tot}, also called force field) consists of additive parameterized two-bodies terms that can be obtained by fitting experimental and/or high-level quantum chemical data into simple functional forms. The AMBER [192,193] and the TIP3P [194] force fields for the proteins and water respectively are used.

For large biological systems, the potential function frequently used takes the form of the summation of different additive terms that correspond to bond distances E_{bonds}, bond angles E_{angles}, bond dihedral $E_{dihedrals}$, van der Waals E_{vdw} and electrostatic E_{elec} interactions (Fig.3.1).

$$E_{tot} = E_{bonds} + E_{angles} + E_{dihedrals} + E_{vdw} + E_{elec}$$

$$\begin{aligned} E_{tot} &= \sum_{bonds} \frac{1}{2} k_r (r - r_{eq})^2 + \\ &+ \sum_{angles} \frac{1}{2} k_\theta (\theta - \theta_{eq})^2 + \\ &+ \sum_{dihedrals} \frac{1}{2} V_n (1 + \cos(n\varphi - \gamma)) + \\ &+ \sum_{i<j}^{atoms} \frac{A_{ij}}{r_{ij}^{12}} - \frac{B_{ij}}{r_{ij}^{6}} + \\ &+ \sum_{i<j}^{atoms} \frac{q_i q_j}{4\pi\epsilon_0 r_{ij}} \end{aligned}$$

Bond stretching and angle bending are represented as harmonic energy terms where r_{eq} and θ_{eq} refer to equilibrium bond lengths and angles, k_r and k_θ are the vibrational constants. The equilibrium values of the bond and angle parameters are usually derived from structural databases, while the force constants are derived from infrared spectroscopy. In the third term, V_n is the torsional barrier corresponding to the n^{th} barrier of a given torsional angle with phase γ: dihedral parameters are calibrated

$$E_{tot} = \sum_{bond} \frac{1}{2} k_r \left(r - r_{eq}\right)^2$$

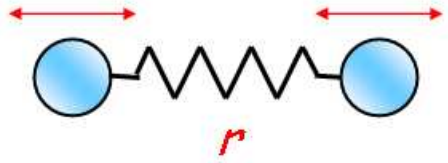

$$+ \sum_{angles} \frac{1}{2} k_\theta \left(\theta - \theta_{eq}\right)^2$$

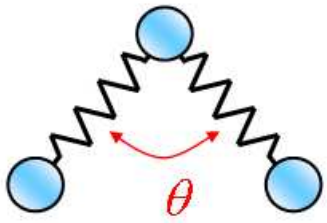

$$+ \sum_{dihedrals} \frac{1}{2} V_n \left[1 + \cos\left(n\varphi + \gamma\right)\right]$$

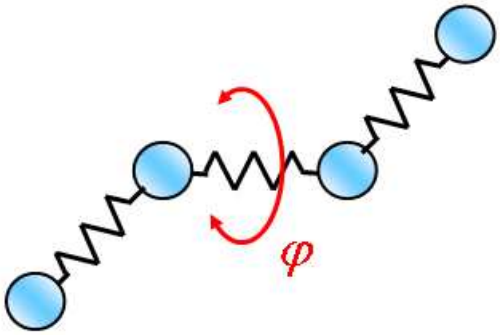

$$+ \sum_{pairs} \left(\frac{A_{ij}}{r_{ij}^{12}} - \frac{B_{ij}}{r_{ij}^{6}} \right)$$

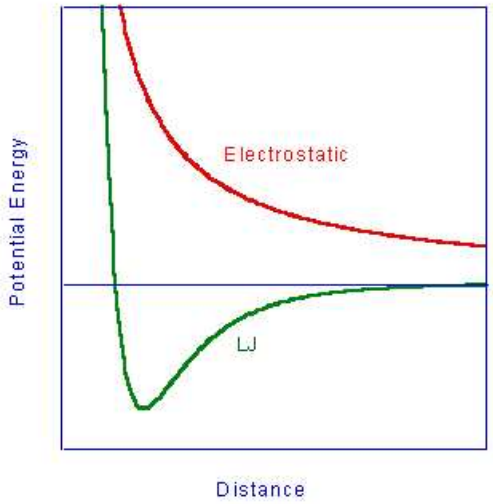

$$+ \sum_{pairs} \frac{q_i q_j}{4\pi\varepsilon_0 r_{ij}}$$

Figure 3.1: The potential energy of the system is expressed as a sum of pairwise additive terms: bond lengths, bond angles, torsional penalties, van der Waals and electrostatic interactions.

on small model compounds, comparing the energies with those obtained by quantum chemical calculations. Improper dihedral angles are added to take into account quantum effects that are not present in E_{tot} as, for example, to preserve planarity in aromatic rings. The last two terms refer to non-bonded van der Waals and electrostatic interactions: the first are described by a Lennard-Jones potential, containing an attractive and a repulsive term, and parameters are defined so as to reproduce chemical-physical properties (e.g., densities, enthalpies of vaporization, solvation free-energies) in organic liquids. The electrostatic energy is evaluated by assuming the dielectric constant ϵ equal to 1, and using the restrained electrostatic potential model (RESP [195, 196]) to define partial atomic point charges: in this model, charges are assigned to the atom-centered points so as to fit the electrostatic potential derived from quantum chemistry calculations for a set of small representative molecules. Van der Waals and electrostatic interactions are calculated between atoms belonging to different molecules or for atoms in the same molecule separated by at least three bonds.

3.1.2 Integration of the equation of motion

The GROMACS program [197] is here used to integrate the equations of motion. During the MD simulations, the system evolves according to the classical Newton equation of motion:

$$\frac{d^2\vec{r}_i(t)}{dt^2} = \frac{\vec{F}_i(t)}{m_i} \quad \text{where} \quad \vec{F}_i(t) = -\frac{dE_{tot}(t)}{d\vec{r}_i}$$

Computing the classical trajectory exactly would require to solve a system of $3N$ second order differential equations, where N is the number of atoms. Actually, these equations are never solved exactly but approximated by a suitable algorithm. For instance, in the popular Verlet algorithm, the positions of each atom are expressed by Taylor expansions whose combination yields an expression for $\vec{r}_i(t + \Delta t)$. The lack of explicit velocities in the Verlet algorithm is remedied by the leap-frog algorithm [198]. Positions at times $t + \Delta t$ and t are given by the Taylor expansions around $t + \Delta t/2$ below:

$$\begin{aligned}\vec{r}_i(t+\Delta t) &= \vec{r}_i(t+\Delta t/2) + \vec{v}_i(t+\Delta t/2)\frac{\Delta t}{2} + \frac{1}{2}\vec{a}_i(t+\Delta t/2)\frac{\Delta t^2}{4} + ... \\ \vec{r}_i(t) &= \vec{r}_i(t+\Delta t/2) - \vec{v}_i(t+\Delta t/2)\frac{\Delta t}{2} + \frac{1}{2}\vec{a}_i(t+\Delta t/2)\frac{\Delta t^2}{4} + ...\end{aligned}$$

whose difference gives:

$$\vec{r}_i(t+\Delta t) = \vec{r}_i(t) + \vec{v}_i(t+\Delta t/2)\Delta t$$

Analogously, an expression for the velocities at half time step is obtained from the expansions around t:

$$\begin{aligned}\vec{v}_i(t+\Delta t/2) &= \vec{v}_i(t) + \vec{a}_i(t)\frac{\Delta t}{2} + ... \\ \vec{v}_i(t-\Delta t/2) &= \vec{v}_i(t) - \vec{a}_i(t)\frac{\Delta t}{2} + ...\end{aligned}$$

whose difference gives:

$$\vec{v}_i(t+\Delta t/2) = \vec{v}_i(t-\Delta t/2) + \vec{a}_i(t)\Delta t$$

The leap-frog algorithm [198] updates both positions and velocities using the forces $\vec{F}_i(t)$ determined by the positions at time t:

$$\begin{aligned}\vec{v}_i(t+\Delta t/2) &= \vec{v}_i(t-\Delta t/2) + \frac{\vec{F}_i(t)}{m_i}\Delta t \\ \vec{r}_i(t+\Delta t) &= \vec{r}_i(t) + \vec{v}_i(t+\Delta t/2)\Delta t\end{aligned}$$

First, the velocities are calculated at half time step, then these are used to calculate the positions at one time step. In this way, positions and velocities leap each other.

The advantage of this algorithm is that velocities are explicitly calculated, and the disadvantage is that they are not calculated at the same time as the positions. As a consequence, kinetic and potential energy cannot directly compute the total energy at time t, but energy evaluation is possible using the following approximate value of velocities at time t:

$$\vec{v}_i(t) = \frac{\vec{v}_i(t - \Delta t/2) + \vec{v}_i(t + \Delta t/2)}{2}$$

3.1.3 Constraint algorithm

The time-step Δt in the integration of the equations of motion is limited by the highest frequency oscillations. These are the bond stretching vibrations, in particular those involving hydrogen atoms, having the highest frequency and a relatively low amplitude. Since these motions are of little interest in most cases, constraining these bond lengths allows to increase Δt with small affects on the accuracy of the simulation, under the assumption that bonds are almost exclusively in their vibrational ground state. Since bonds in molecules are coupled, resetting coupled constraints after an unconstrained update is a nonlinear problem.

The LINCS algorithm satisfies a set of holonomic constraints by an efficient parallelizable matricial representation of the equations [199].

3.1.4 Periodic boundary conditions

MD simulations are usually performed under periodic boundary conditions, to minimize boundary effects and to mimic the presence of the bulk. In this approach, the system containing the N atoms is replicated in all directions to yield an infinite periodic lattice of identical cells (Fig.3.2). When a particle moves in the central cell, its periodic image in every other cell moves accordingly. As one molecule leaves the central cell, its image enters from the opposite side without any kind of interactions with the cell boundary. Following the so called minimum image convention, only the nearest image of each particle is considered when calculating non-bonded interactions. This implies that

the cutoff radius used to truncate non-bonded interactions must not exceed half the shortest box vector, otherwise more than one image would be within the cutoff distance of the force.

$$\text{cutoff} < \frac{\min(a, b, c)}{2}$$

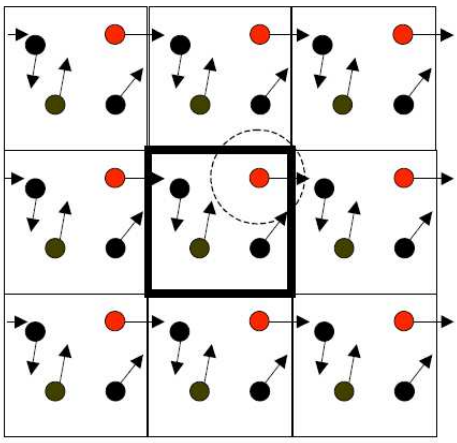

Figure 3.2: Periodic boundary conditions: the MD system is surrounded by translated copies of itself.

3.1.5 Long-range interactions

In a many-particle computational system, interactions may be divided in two groups: bounded (bonds, angles and dihedral) and non-bonded (vdW and electrostatics). While the bonded interactions are intrinsically short-range, non-bonded terms extend to the infinity (long-range interactions). Nevertheless, the vdW interactions can be treated only as short-range interactions, because their energy function decays rapidly; in fact, although these potential functions are not rigorously zero at any distance, the cutoff truncation will result in a negligible systematic error. For Coulombic interactions, on the contrary, the cutoff truncation introduces energetic discontinuities which cause instabilities of the simulation, as the electrostatic potential function goes slowly to zero. This problem has been faced with the use of smoothing functions or the twin-range cutoff method. More rigorously, interactions with all periodic images must be explicitly

considered: the Ewald summation method [200] is used in classical MD to face this computational task.

The total electrostatic energy of N particles and the periodic images is given by

$$V = \frac{1}{8\pi\epsilon_0} \sum_{\vec{n}}^{*} \sum_{i=1}^{N} \sum_{j=1}^{N} \frac{q_i q_j}{|\vec{r}_{ij,\vec{n}}|}$$

where $\vec{n}$ is the box index vector and the star indicates that terms with $i = j$ should be omitted when $|\vec{n}| = 0$. This sum is conditionally convergent.

Ewald summation is a technique for computing the interaction of a set of charges and all its periodic images. The charge distribution in the system is a set of point charges, represented as delta functions:

$$\rho(\vec{r}) = \Sigma_i q_i \delta(\vec{r} - \vec{r}_i)$$

In the Ewald method, each q_i charge of the distribution $\rho(\vec{r})$ is screened by a diffuse charge distribution $\rho_i^G(\vec{r})$ of the opposite sign, such that the total charge of this cloud exactly cancels q_i.

$$\rho_i^G(\vec{r}) = -q_i(\alpha/\sqrt{\pi})^3 e^{-\alpha 2|\vec{r}-\vec{r}_i|^2}$$

$$\rho^G(\vec{r}) = \sum_i \rho_i^G(\vec{r})$$

Each point charge q_i is now surrounded by an isotropic Gaussian charge distribution $\rho_i^G(\vec{r})$ of equal magnitude and opposite sign, which screens the interaction between the point charges, so that the interaction calculated using the screened charge distribution $\rho(\vec{r}) + \rho^G(\vec{r})$ becomes short-ranged. The interaction energy reads:

$$E_{[\rho(\vec{r})+\rho^G(\vec{r})]} = \frac{1}{8\pi\epsilon_0} \sum_{\vec{n}}^{*} \sum_{i=1}^{N} \sum_{j=1}^{N} \frac{q_i q_j}{|\vec{r}_{ij,\vec{n}}|} f^{er}(\alpha|\vec{r}_{ij,\vec{n}}|)$$

where

$$f^{er}(x) = 2\pi^{1/2} \int_x^\infty e^{-y^2} dy$$

To restore the initial system, an anti-screening Gaussian charge distribution $-\rho^G(\vec{r})$, centered at the position of each atom i with the same charge of q_i, is added. The potential energy of this Gaussian charge distribution is calculated by a converging Fourier series in the reciprocal space [200].

The parameter α is tuned in order to optimize convergence properties of both summations. In particular, in the particle mesh Ewald method [201, 202, 203], α is chosen sufficiently large so that interactions between atom pairs for which $|\vec{r}_{ij,\vec{n}}|$ exceeds a specified cutoff are negligible in the direct space sum and the reciprocal space sum is approximated by an interpolation of the potential on a grid.

3.1.6 Thermostats

Among the several methods to control the temperature usually available in MD software packages, the weak coupling method (Berendsen thermostat [204]) and the coupling to an external bath algorithm (Nosé Hoover thermostat [205, 206]) are used here.

In the weak coupling method [204], the temperature of the system $T(t)$ is kept close to the target temperature T_0 by the equation:

$$\frac{dT(t)}{dt} = \frac{T_0 - T(t)}{\tau_T}$$

where $T(t)$ is the instantaneous temperature, T_0 is the reference temperature and τ is the coupling time constant. The instantaneous temperature $T(t)$ of a system with N_{df} degrees of freedom is related to the kinetic energy $E_{kin}(t)$:

$$E_{kin}(t) = \sum_{k=1}^{N} \frac{1}{2} m_k v_k^2(t) = \frac{1}{2} N_{df} k_B T(t)$$

The atomic velocities can then be scaled by a factor $\lambda(t)$ as follows:

$$\delta E_{kin}(t) = [\lambda(t)^2 - 1]\frac{1}{2}N_{df}k_B T(t)$$

Since:

$$\delta E_{kin}(t) = N_{df}c_V \delta T(t)$$

then:

$$\lambda(t) = \sqrt[2]{1 + \frac{2c_V dt}{k_B \tau_T}\frac{T_0 - T(t)}{T(t)}}$$

where c_V is the heat capacity per degree of freedom. The factor $\lambda(t)$ is used to scale the velocities v_k at each integration step dt, in order to relax the temperature toward the target temperature value T_0. The relaxation rate is controlled by the time coupling constant τ_T, which should be small enough to achieve the required temperature and large enough to avoid disturbance of the physical properties of the system by coupling to the bath.

Even though the Berendsen weak coupling algorithm is efficient for relaxing the system to the target temperature, it does not allow for a proper sampling of the canonical ensemble. Canonical ensemble simulation is enabled by employing the Nosé-Hoover thermostat.

In the Nosé-Hoover approach [205, 206], the ensemble is extended by introducing a thermal reservoir and a friction term in the equations of motion.

$$\frac{d^2\vec{r}_i}{dt^2} = \frac{\vec{F}_i}{m_i} - \xi(t)\frac{d\vec{r}_i}{dt}$$

The friction force is proportional to the product of each particle's velocity and a friction parameter $\xi(t)$. This friction parameter is a fully dynamic quantity with its own equation of motion.

$$\frac{d\xi(t)}{dt} = \frac{T(t) - T_0}{Q}$$

The time derivative is calculated from the difference between the current temperature $T(t)$ and the reference temperature T_0, and Q determines the strength of coupling to the heat bath.

3.1.7 Barostats

To closer resemble biological systems, the pressure can be controlled by applying a pressure coupling algorithm, as the Berendsen [204] and the Parrinello-Rahman methods [207].

The Berendsen algorithm scales the coordinates and the box vectors: the effect is a first-order kinetic relaxation of the instantaneous pressure $\mathbf{P}(t)$ toward the reference pressure $\mathbf{P}_0$, with a time constant τ_P that can be specified as an input parameter. Similarly to the temperature weak coupling algorithm:

$$\frac{d\mathbf{P}(t)}{dt} = \frac{\mathbf{P}_0 - \mathbf{P}(t)}{\tau_P}$$

and the scaling factor $\mu(t)$ for atoms positions is:

$$\mu_{\alpha\beta} = \delta_{\alpha\beta} - \beta_{\alpha\beta}\frac{\Delta t}{3\tau_P}[P_{0,\alpha\beta} - P_{\alpha\beta}(t)]$$

where β is the isothermal compressibility, $\mathbf{P}(t)$ is the instantaneous pressure, $\mathbf{P}_0$ is the target pressure and τ_P is the pressure coupling time constant.

In the Parrinello-Rahman algorithm, similarly to the Nosé-Hoover temperature coupling, the equations of motion are modified:

$$\frac{d^2\vec{r}_i}{dt^2} = \frac{\vec{F}_i}{m_i} - \mathbf{M}(t)\frac{d\vec{r}_i}{dt}$$

The coupling matrix $\mathbf{M}(t)$ is determined by providing the reference pressure $\mathbf{P}_0$, the isothermal compressibility β and the pressure time constant τ_P as input parameters, in the following way:

$$\mathbf{M}(t) = \mathbf{b}^{-1}\left[\mathbf{b}\frac{d\mathbf{b}'}{dt} + \frac{d\mathbf{b}}{dt}\mathbf{b}'\right]\mathbf{b}'^{-1}$$

and:

$$\frac{d\mathbf{b}^2}{dt^2} = V\mathbf{W}^{-1}\mathbf{b}'^{-1}(\mathbf{P} - \mathbf{P}_0)$$

where V is the box volume and $\mathbf{W}$ is a matrix parameter that determines the strength of the coupling:

$$(\mathbf{W}^{-1})_{\alpha\beta} = \frac{4\pi^2\beta_{\alpha\beta}}{3\tau_p^2 L}$$

where L is the largest box matrix element.

3.1.8 Generalized Born model

The Generalized Born (GB) model is an implicit solvent model that can be used to run significantly faster MD simulations than those which make use of explicit solvent [208, 209]. However, due to the crucial role of the solvent, the GB approach usually provides only qualitative insights.

In the GB model, the apolar contribution to the protein-solvent interaction is estimated as linearly dependent on the solvent accessible surface area of the protein; the polar term, which takes into account also salt effects, reads:

$$\Delta G_{pol}^{GB} = -\frac{1}{2}\sum_{i,j}\frac{q_i q_j}{f_{GB}(r_{ij},\alpha_i,\alpha_j)}(1 - \frac{e^{-\kappa f_{GB}(r_{ij},\alpha_i,\alpha_j)}}{\varepsilon_w})$$

where κ is the Debye-Hückel screening parameter; α_i is the effective Born radius of atom i, which reflects the degree of its burial inside the molecule; f_{GB} is a function that interpolates between the effective Born radius α when $r_{ij} \to 0$ and an effective pairwise interaction distance [209, 210]:

$$f_{GB} = \sqrt{r_{ij}^2 + \alpha_i \alpha_j \exp(-r_{ij}^2 / 4\alpha_i \alpha_j)}$$

3.1.9 Steered molecular dynamics

Many biological processes are characterized by high energy barriers and occur in time-scales that are not feasible by current computational techniques. Nevertheless, their study by means of MD simulations would provide valuable information. To overcome the energy barriers and thus to speed up the simulations, an external force is applied to a selected group of atoms to steer the system along a particular degree of freedom. This allows to focus the simulation on a particular dynamic event, reducing the amount of computational expense [211, 212, 213, 214, 215, 216, 217, 218, 219].

Steered Molecular Dynamics (SMD) is here applied to investigate the unbinding of ligand/receptor complexes: the ligand is harmonically restrained to a point that moves away from the receptor mass center with constant velocity $\vec{v^r}$. The force $\vec{F^r}$ applied to the ligand is:

$$\vec{F^r} = k^r \cdot (\vec{x_0^r} + \vec{v^r} t - \vec{x^l}_{cm})$$

where k^r is the restraint force constant, $\vec{x^r}_0$ is the initial position of the restraint point and $\vec{x^l}_{cm}$ is the position of the ligand mass center. It should be stressed that, in general, only qualitative information about binding paths and intermediate states can be obtained.

3.1.10 Analysis of MD trajectories

The general flowchart of an MD run is:

1. reading the initial conditions, i.e. the positions and velocities of the atoms;
2. reading the parameters of the simulation (temperature and pressure, control algorithms, time step, special features);
3. computing the total force that acts on each atom;
4. updating the coordinates and the velocities of the atoms by the integration of the Newton equation of motion;
5. back to point 3.

Data from MD trajectories can be used to calculate several structural and dynamic properties.

Displacement

The conformational stability of a macromolecule can be estimated by the Root Mean Square Displacement (RMSD). The RMSD of a set of N atoms at time t, with respect to the initial conformation, reads:

$$\mathrm{RMSD}(t) = \sqrt{\frac{\sum_{i=0}^{N} |\vec{r}_i(t) - \vec{r^0}_i|^2}{N}}$$

where $|\vec{r}_i(t) - \vec{r^0}_i|$ is the displacement of the i^{th} atom at time t from the reference position $\vec{r^0}_i$. An increase of the RMSD indicates that the protein moves to a conformation different from the initial structure and thus suggests an incomplete sampling or a conformational change.

Fluctuation

The Root Mean Square Fluctuation (RMSF) is computed for each atom i:

$$\mathrm{RMSF}_i = \sqrt{\langle(\vec{r}_i - \langle\vec{r}_i\rangle)^2\rangle}$$

where $\vec{r}_i$ is the position vector of the i^{th} atom and the brackets stand for a temporal average. This quantity can be compared to crystallographic B-factor B_i through the relation:

$$B_i = 8\pi^2 \mathrm{RMSF}_i^2/3$$

The RMSF analysis provides information about the atomic fluctuations throughout the simulation and thus indicates the most flexible regions of the protein.

Contact surface

The Contact Surface (CS) between two groups of atoms is estimated as the difference between the Solvent Accessible Surface Areas (SASA) of the two groups separated and in the complex, assuming no conformational change. SASA is calculated using the center-probe area definition [220] and 0.14 nm solvent probe radius [221, 222]. CS provides a rough estimate of the non-polar contribution to the binding free energy [223].

Large-scale collective motions

The description of the protein dynamics in terms of collective motions is particularly useful to dissect from an MD trajectory the structural low frequency vibrations, which are often relevant for the protein function. To identify the concerted large-scale structural fluctuations occurring in a protein, the degree of correlation of pairs of residues is calculated in the covariance matrix C, whose elements are:

$$C_{ij} = \langle(\vec{r}_i - \langle\vec{r}_i\rangle) \cdot (\vec{r}_j - \langle\vec{r}_j\rangle)\rangle$$

where $\vec{r}_i$ is the i^{th} atom position and the brackets indicate temporal average.

Large-scale motions can be calculated as eigenvectors of the $C\alpha$ atoms covariance matrix. The symmetric matrix can be diagonalized by an orthonormal coordinate transformation R which transforms C into a diagonal matrix Λ of $3N$ eigenvalues λ_i:

$$R^T C R = \Lambda$$

The columns of R are the eigenvectors or Essential Modes (EM) and the eigenvalues λ_i are the variance in the direction of the corresponding EM. The covariance analysis defines a new coordinate system for the data set, in which the new coordinates are uncorrelated [224, 225, 226, 227, 228]. The six roto-translational degrees of freedom can be eliminated by performing a RMSD fit between each MD snapshot and the initial configuration before calculating C.

Eigenvectors are ordered with decreasing eigenvalues, which are proportional to the percentage of total fluctuation the corresponding EM describes ($\lambda_i / Tr\ \Lambda$). Usually, it turns out that most of the total motion is spanned over the first few eigenvectors. The amount of motion covered by a subset of EMs is the summation of the corresponding eigenvalues λ_i divided by the trace of Λ.

The principal component of a EM is the projection of the trajectory on the eigenvector. It has been proven that the principal components of random diffusion are cosines with the number of periods equal to half the principal component index [227]. The cosine content analysis is used to check whether the EMs obtained from the diagonalization of the covariance matrix C resemble those of random diffusion.

3.2 Elastic network analysis

The capabilities of actual computer power allows, within a reasonable cost, to follow the dynamic evolution of few hundred residues large proteins for tens of nanoseconds. The large-scale dynamic features encountered in MD trajectories can be interpreted as a superposition of independent harmonic modes that can be achieved by simply substituting detailed force-field interactions by harmonic couplings, provided that the protein fluctuates around the initial conformation and that the protein does not undergo large conformational changes toward a more stable structure [229].

In the coarse-grain Gaussian network model the protein is described at the residue level and the interaction between couples of residues is described by simple harmonic terms [230, 229, 231] (Fig.3.3). Here, the so-called β-Gaussian model is used: in this model, centroids tethered to the Cβ atoms are introduced to mimic the side-chains. This allows a better modeling of the directionality of pairwise interactions in the protein and leads to an improved vibrational description [9]. The E_{tot} of a protein is described as an expansion in terms of deviations of the amino acids from their reference positions. All couples of residues within a given cutoff value interact and, to account for the higher strength of the peptide bonds with respect to non-covalent interactions between amino acids, an explicit chain term has been added. By construction, the global minimum of E_{tot} coincides with the native state.

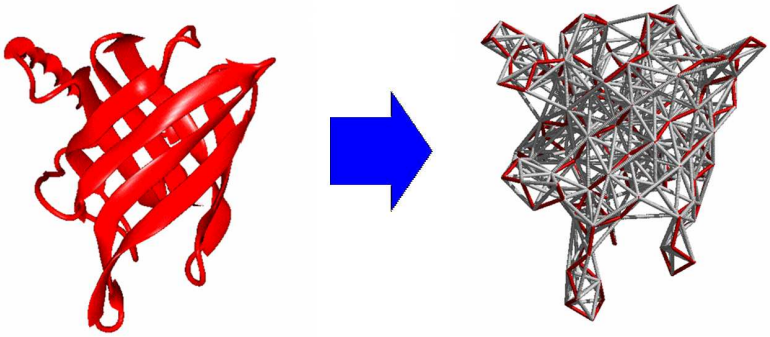

Figure 3.3: The protein structure is modeled as an elastic network in which pairs of Cα and Cβ atoms are connected by springs

The elastic response of the system is uniquely dictated by the eigenvalues and eigenvectors of the covariance matrix. The main observable quantity that can be calculated within the Gaussian model is the correlation between displacements of pairs of Cα's atoms. The eigenvectors of the covariance matrix represent the three-dimensional independent modes of structural distortion for the protein.

3.3 Electrostatic calculations

Insights into the electrostatic interactions in proteins can be obtained with the Poisson-Boltzmann equation [189]. In this approach, the solvent is represented as continuum and the electrostatic potential $\Psi(r)$ can be determined by solving the following equation:

$$\vec{\nabla} \cdot \left(\varepsilon(\vec{r}) \vec{\nabla} \Psi(\vec{r}) \right) = -4\pi \rho^f(\vec{r}) - 4\pi \sum_i c_i^\infty z_i q \exp\left(\frac{-z_i q \Psi(\vec{r})}{k_B T} \right) \lambda(\vec{r})$$

where $\rho^f(\vec{r})$ is the fixed charge distribution of the molecule, $\varepsilon(\vec{r})$ is the position dependent dielectric constant, c_i^∞ is the concentration of ion i at an infinite distance from the molecule, z_i is its valency, q is the proton charge, k_B is the Boltzmann constant, T is the temperature and $\lambda(\vec{r})$ describes the accessibility to ions at point $\vec{r}$.

An analytical solution of the equation can be obtained only for very simple geometries and charge distributions. For proteins, the equation can be solved numerically by the finite difference methods on a grid. As a first step, the molecular surface is generated using a spherical probe of 1.4 Å, which is the water radius. A grid is generated and, according to the surface, a high dielectric constant value is then assigned to the grid points that lie on the external side of the macromolecule, which are supposed to belong to the solvent, and a low dielectric constant value is assigned to the remaining grid points. Each atom charge is split to the nearest grid points of the mesh and a smoothing algorithms is used to improve the results. The electrostatic potential is finally numerically estimated for each grid point and the energy of the charged grid is calculated. Since every atom charge is split to different grid points, different parts of the charge of the same atom interact each other. The self-grid energy is removed in the difference between energies obtained for the same protein conformation with the same grid in different conditions.

Here, the Poisson-Boltzmann equation is numerically solved using the APBS program [232].

3.4 Hot spot binding energy prediction

Residues at the protein/protein interface that contribute significantly to the complex stability and whose mutation can affect the interaction are defined as hot spots binding energy. With the Baker et al.'s computational alanine scanning procedure [190, 191] we estimate the residues at the protein/peptide interface which form interactions important for the complex stability. To this aim, the predictor calculates the residues at the interface which significantly destabilize the complex when mutated to alanine, estimating both the van der Waals and the electrostatic contributions to the free energy of binding, based on an all-atom rotamer description of the side chains together with an energy function dominated by Lennard-Jones interactions, solvation effects and hydrogen bonding [190, 191]. Binding energy hot spots are here defined for residues whose $\Delta\Delta G_B^{hs} \geq 2kT$.

Chapter 4

Catabolite Activator Protein

The Catabolite Activator Protein (CAP, also called cAMP-Receptor-Protein) is a bacterial DNA-binding protein involved in the activation of the transcription of several operons [30,37,33]. Cyclic Adenosine MonoPhosphate (cAMP) binding to CAP causes a cascade of structural rearrangements that allows for selective binding to DNA (consensus sequence is 5'-AAATGTGATCT-3') [59, 31, 32]. This in turn induces DNA bending [43, 60, 61, 63, 64] and a rearrangement of CAP [69, 70], which is followed by the binding of the RNA polymerase enzyme [66, 67, 68].

The X-ray structures of DNA-bound and DNA-free states of CAP have provided key insights on the molecular basis of DNA binding [41, 43, 44, 23]. These studies show that CAP is a homodimer whose subunits (namely "A" and "B", Fig.1) are formed by two domains. The first is the conserved signaling module N-terminal Cyclic Nucleotide Binding Domain (CNBD, residues 1-137) [46], which includes an eight-stranded β-roll flanked by an α-helix (A-helix) at its N-term, and by two helices (B and C helices) at its C-term. A hinge region, which is close to the homodimeric symmetry axis (residues 133-142), connects the CNBD to the C-terminal DNA-Binding Domain (DBD, residues 138-209). The latter includes a helix-turn-helix motif that binds to DNA, inducing a final bent of $\sim 90^\circ$ [43]. Two cAMP binding sites for each subunit are present. The primary binding site, which has a μM affinity for cAMP [35, 40], is located in the CNBD, within the β-roll, and it is lined by the C-helices of both subunits: binding of cAMP (in its *anti* conformation) triggers a reorientation of the $\beta 4/\beta 5$ loops and of the C-helices, which leads to an allosteric change of the hinges that repositions the DBDs

and results in DNA binding [49, 50, 51, 52, 53, 54, 55, 23, 45, 56, 57, 46, 58]. Selectivity toward the target DNA sequence is achieved by cAMP binding to the primary sites [35]. The secondary binding site, with mM affinity for cAMP that binds in its *syn* conformation, is formed by residues from both domains of the same subunit and from the hinge region of the opposite subunit [44]. DNA binding to CAP depends on cAMP concentration [38, 39, 35, 40].

In the crystal phase, the structures of the subunits have been found to depend on the state of the protein. In the DNA-bound state, the DBDs are symmetrically arranged and are both packed against their CNBDs (*closed* conformation for both subunits, Fig.4.1) [41, 43, 44]. In the DNA-free X-ray structure, one subunit is in the *closed* conformation, whilst the other is separated from its corresponding CNBD by a cleft (*open* conformation, Fig.4.1) [23]. It is well known that crystal packing forces may induce structural modifications in proteins [233, 234]: therefore, the structure of such subunits in aqueous solution might differ significantly from that in the crystal. As shown in Fig.4.1, in the X-ray structure several DBD residues exhibit close contacts with other proteins. Therefore the crystal packing could be responsible for possible deviations from the biologically relevant protein conformation. Here we address this issue by undertaking a comparative MD study of the protein in the crystal phase and in aqueous solution.

Our MD calculations of the crystal turn out to reproduce the structure of the protein experimentally observed (in particular the *closed-open* conformation, Fig.4.1), suggesting that our computational setup provides a relatively accurate description of the system. In addition, the ligand bound protein in solution assumes an *open-open* symmetric conformation (Fig.4.1). Such conformation could play a key role for DNA molecular recognition.

4.1 Computational Details

The following models are constructed: (i) $\mathbf{CAP_{cryst}}$ is the X-ray structure from *Escherichia coli* solved at a resolution of 2.10 Å (pdb entry code 1G6N [23], Fig.4.1); (ii) $\mathbf{CAP_{aq}}$ is based on the same X-ray structure [23], although one asymmetric unit

is considered (Fig.4.1); (iii) $\mathbf{CAP^{*}_{aq}}$ is the protein in aqueous solution obtained by removing the DNA from the X-ray structure of the CAP-DNA complex from *Escherichia coli* solved at a resolution of 2.80 Å (pdb entry code 1O3T [44], Fig.4.1 and Fig.4.3). In all systems, cAMP is bound to both CNBDs, acid and basic residues are assumed to be ionized at the physiological conditions; hydrogens are added by assuming standard bond lengths and angles. Sodium ions are added to achieve neutrality (Tab.4.1).

Solvation. $\mathbf{CAP_{aq}}$ and $\mathbf{CAP^{*}_{aq}}$ are solvated by adding a water model with 1.0 Kg/l density into the parallelepiped simulation boxes that contain the different solutes. Solvent molecules are rejected if the distance between any solvent atom and the closest solute atom is lower than the sum of their respective van der Waals radii. This procedure generates around the solute small voids that are filled after a short solvent simulation (i.e. 60 ps of MD using the Berendsen thermostat and barostat [204] with T=300 K, P=1 atm and 1 ps time constants) with a reduction of the MD box volume. The protein in the crystal lattice solvated using the procedure described above shows several cavities which could be filled by water. Test MD calculation on such system results in a small shrinking of the cell lattice, although the protein structure is maintained (see Supplementary Information). Thus, a different solvation procedure is used for $\mathbf{CAP_{cryst}}$. We define a grid of $\backsim$0.29 nm size spanning the entire unit cell and water oxygens are placed at any grid point if the corresponding grid cell is empty, i.e. if no solute atom is found in the given cell. The solvent equilibration dynamics (60 ps) is sufficient to restore the normal water structure as confirmed by a comparison with the crystal solvated with the standard procedure outlined above (Data not shown).

Complex name	based on	x (nm)	y (nm)	z (nm)	n° of a.a.	n° of cAMP	n° of waters	n° of Na+
$\mathbf{CAP_{aq}}$	1G6N [23]	7.40	9.15	8.52	401	2	16,954	2
$\mathbf{CAP^{*}_{aq}}$	1O3T [44]	8.99	7.05	9.09	396	2	16,995	0
$\mathbf{CAP}_{cryst}$	1G6N [23]	4.68 (=)	9.55 (-0.01)	10.54 (-0.01)	1604	8	8000	8

Table 4.1: **Selected features from our MD calculations.** The table shows the pdb entry codes of the initial, X-ray structures, the mean dimensions of the MD unit cell after equilibration and the number of amino acids, cAMP molecules, water molecules and sodium ions, which are added to neutralize the box. In $\mathbf{CAP}_{cryst}$, the differences between theoretical and experimental values of the cell parameters are reported in brackets.

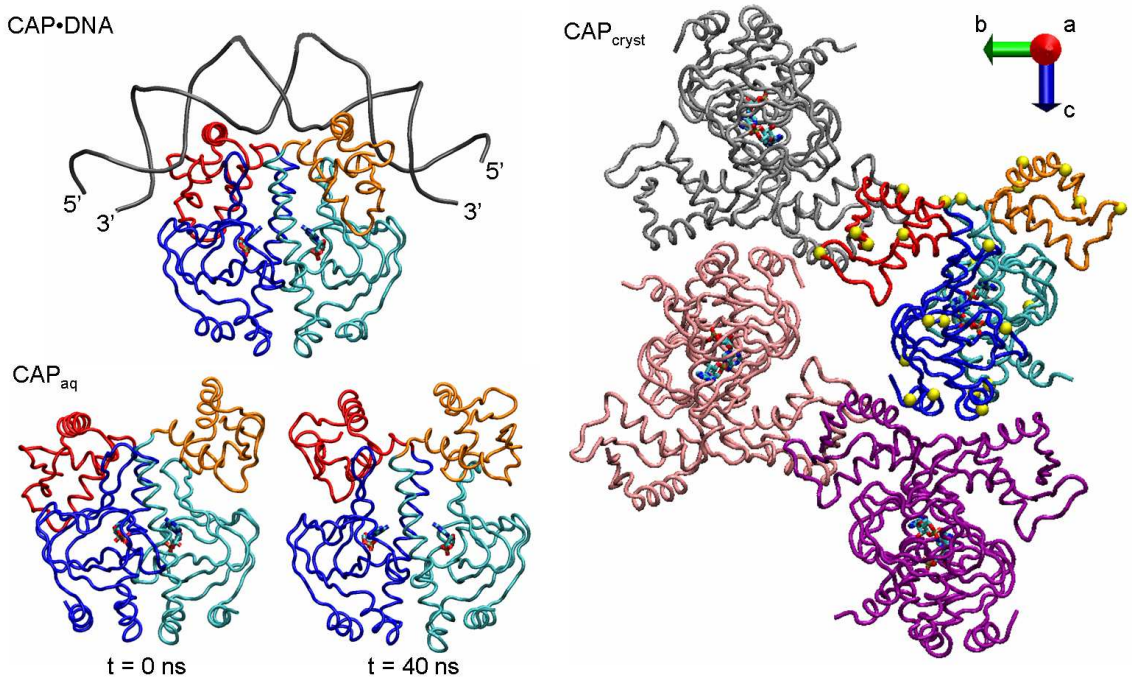

Figure 4.1: **Structures of CAP.** The asymmetric unit of the DNA-bound CAP x-ray structure (**CAP·DNA**) [44], the unit cell of the DNA-free CAP in the crystal lattice (**CAP**$_{cryst}$) [23] and CAP in aqueous solution (**CAP**$_{aq}$) in the initial and in the final MD conformations are reported as ribbons. Water molecules are not shown for clarity. The CNBD and the DBD of subunit "A" are colored in blue and red, respectively, while the same domains of subunit "B" are colored in cyan and orange, respectively; the cAMP molecules are drawn in sticks and colored by the atom type; DNA (sequence 5'-GCGAAAAATGCGATCTAGATCGCATTTTTCG-3') is represented as gray double strand. In **CAP**$_{cryst}$, one asymmetric unit, which is rotated with respect to the other panels, is colored as above and the yellow spheres indicate the residues forming crystal packing contacts (interresidue distance between non-hydrogen atoms smaller than 0.35 nm); the remaining three proteins are shown in different colors; the directions of the three cell vectors are also reported. Figures obtained with the VMD program [235].

Molecular dynamics. We use the AMBER94 force field [192, 193] for protein, DNA and ions and the TIP3P force field [194] for water. The force field for cAMP is developed in ref. [236] and is proven to reliably reproduce the molecule interactions within several cAMP binding proteins [236, 47, 48].

Rectangular periodic boundary conditions are applied. The particle mesh Ewald method is used to evaluate long range electrostatics [202, 203, 201]. A cutoff of 1 nm is used for the real part of the electrostatic and for the van der Waals interactions. The minimum distances between the periodic images of the complexes in solution turn out to be always greater than the short range interactions cutoff. Constraints are applied to all chemical bonds using the LINCS algorithm [199]. The integration time step is set to 1.5 fs.

After an energy minimization and 60 ps of solvent simulation, using the Berendsen thermostat and barostat [204] (T=300 K and P=1 atm), Molecular Dynamics (MD) simulations are performed in the NPT ensemble, using the Nosé-Hoover thermostat [206, 237] and the Parrinello-Rahman procedure [207, 205] (T=300 K and P=1 atm); the pressure coupling is isotropic. $\mathbf{CAP_{aq}}$, $\mathbf{CAP^{*}_{aq}}$ and $\mathbf{CAP_{cryst}}$ are simulated for 40, 15 and 15 ns of MD, respectively. The calculations are performed using the GROMACS program [238, 197].

Snapshots collected every 15 ps are analyzed to obtain the following properties: (i) Root Mean Square Deviations (RMSD) of the Cα atoms are calculated after least square fit to the respective X-ray structure [23, 44], if not otherwise specified; (ii) Essential Mode (EM) analysis of the Cα atoms is used to identify large collective motions [226, 239, 225, 227, 228].

Electrostatics. The Poisson-Boltzmann equation [189, 240] is used to calculate the electrostatic potential on and outside the protein surface, using the APBS program [232]: a 2 runs focusing procedure is applied with 0.06 nm final grid spacing; 100 mM monovalent ionic concentration, 300 K temperature, protein dielectric constant $\epsilon_{in} = 1$ and solvent dielectric constant $\epsilon_{wat} = 80$ are assumed. The calculations are carried out on the protein as in the initial conformation in the $\mathbf{CAP^{*}_{aq}}$ MD system and as after 40 ns of MD in the $\mathbf{CAP_{aq}}$ MD system (*closed* and *open* conformations, respectively).

4.2 Results and discussion

CAP_{cryst}. In the X-ray structure of the DNA-free, cAMP-bound CAP [23], several crystal packing contacts, i.e. contacts between residues from different asymmetric units, are observed. They involve residues spread throughout the protein structure (Tab.4.2 and Fig.4.1). Here we perform 15 ns of MD simulation to check whether our computational setup (see Computational Details section) is able to reproduce the determinants of the X-ray structure.

Residue		Subunit	Residue		Subunit
GLU	12	A	ARG	185	B
HIS	19	A	GLU	55	B
SER	27	A	GLU	37	B
THR	28	A	GLU	37	B
VAL	43	A	ARG	185	B
GLU	55	A	HIS	31	B
GLU	81	A	HIS	21	B
GLN	104	A	ASP	138	A
PRO	160	A	ARG	180	B
ARG	169	A	PRO	160	B
ARG	185	A	GLN	107	B
ARG	185	A	PRO	110	B
GLY	200	A	ASN	194	B
LYS	201	A	ASN	194	B
LYS	201	A	TYR	206	B

Table 4.2: **Crystal packing contacts in CAP_{cryst} [23].** Contacts are defined for couples of residues from different asymmetric units with non-hydrogen atoms closer than 0.35 nm.

To characterize the *closed* (subunit "A", colored in blue and red in Fig.4.1) and the *open* (subunit "B", colored in orange and cyan in Fig.4.1) states, we monitor the distances between the mass centers of the DBD and CNBD of the same subunit (2.66 nm and 2.92 nm, respectively in the initial structure). The calculated values are 2.61 (0.06) nm and 2.98 (0.05) nm (Fig.4.2d), in good accord with the experimental data. The RMSDs of the unit cell and for the four homodimers are 0.16 (0.03) nm and 0.13 (0.02) nm, respectively (Fig.4.2a). Finally, our calculations turn out to reproduce the experimental unit cell parameters within 0.01 nm (Tab.4.1). [1] We conclude that our calculations are able to reproduce the X-ray structure determinants.

[1]Notice that using a lower number of water molecules causes a decrease of the calculated unit cell parameters in the NPT MD simulation.

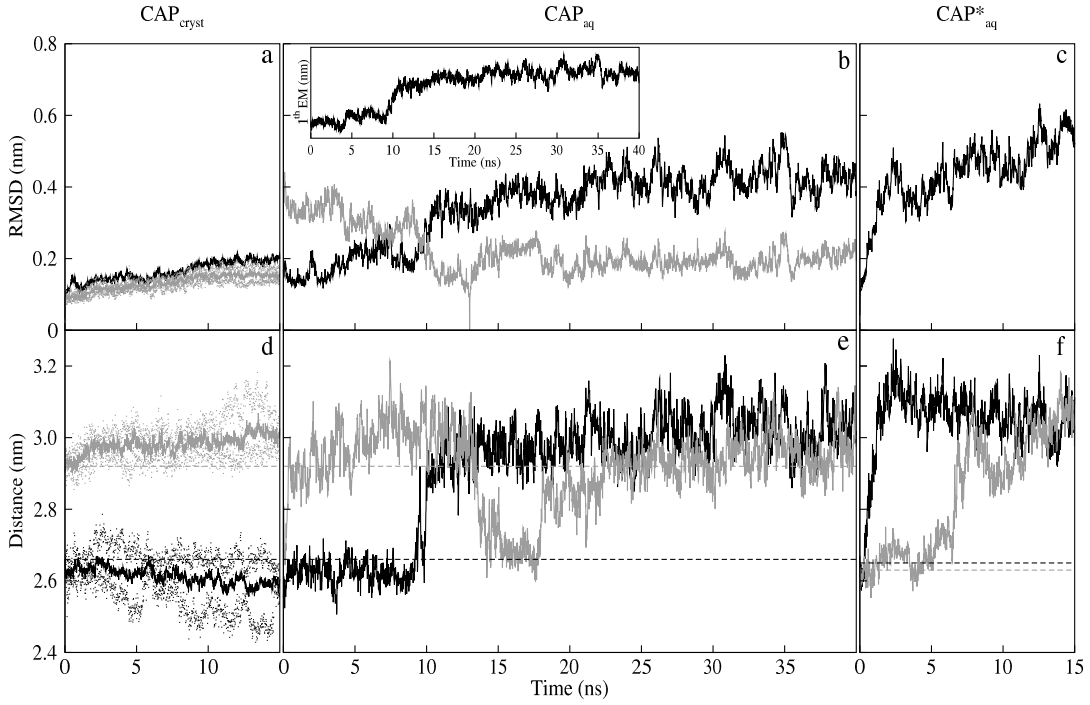

Figure 4.2: **MD simulations.** (a-c) RMSD of the $\mathbf{CAP_{cryst}}$, $\mathbf{CAP_{aq}}$ and $\mathbf{CAP^{*}_{aq}}$ plotted as a function of the simulation time (black lines). In (a), the RMSD is also averaged over the four proteins in the unit cell, considering each molecule separately, and extreme values are reported as dots (gray line). In (b), RMSD are also calculated using the structure after 13 ns of MD as the reference conformation (gray line); the inset shows the principal component of the EM with the highest eigenvalue. (d-f) Distances between CNBD and DBD mass centers in subunits "A" and "B" (solid and gray lines, respectively) of CAP in the $\mathbf{CAP_{cryst}}$, $\mathbf{CAP_{aq}}$ and $\mathbf{CAP^{*}_{aq}}$, plotted as a function of the simulation time. Initial distances are indicated by the horizontal dashed lines. In (d), distances are averaged over the 4 asymmetric units of the unit cell and extreme values are indicated by dots.

$\mathbf{CAP_{aq}}$. We now relax the CAP structure in aqueous solution. One of the four asymmetric units in the X-ray structure [23] is immersed in a $\backsim$17,000 molecules water box (Tab.4.1) with 2 sodium counterions. The system then undergoes 40 ns of MD simulation. During the dynamics, the RMSD fluctuates at $\backsim$0.2 nm in the first part of the simulation and increases at $\backsim$0.4 nm after 10 ns (Fig.4.2b), indicating the presence of a transition. The protein moves to a conformation in which the DBD of subunit "A" is separated from the respective CNBD by a cleft, as initially observed in subunit "B". To filter the large scale concerted structural rearrangements from small harmonic fluctuations, we use Essential Mode (EM) analysis [226,239,225,227,228]. This method consists in a diagonalization of the covariance matrix of atomic fluctuations: eigenvec-

tors are ordered with decreasing eigenvalues, which are proportional to the percentage of total fluctuation the corresponding EM describes. Therefore, the eigenvector with the highest eigenvalue describes the collective motion that most accounts for the structural fluctuations. In our case, the conformational transition featured by the DBD of subunit "A" is described by the first EM, whose eigenvalue accounts for $\backsim$ 60% of the total motion of the protein, with a cosine content of 0.69 [225, 227, 228]. Indeed, the projection of this eigenvector on the Cartesian trajectory closely resembles the RMSD trace. It reaches a plateaux within 13 ns (Fig.4.2, inset) and correlates with the increase of the distance between the mass centers of the two domains of subunit "A" (Fig.4.2e and animation at http://www.sissa.it/$\sim$berrera/CAP.html). The protein then fluctuates around the new symmetric *open* conformation: in fact, in the last 27 ns of MD, the RMSD calculated using as the reference structure the conformation after 13 ns (available at http://www.sissa.it/$\sim$berrera/CAP.html) is $\backsim$0.2 nm (Fig.4.2b) and the mean distances between intrasubunit DBD and CNBD mass centers are 3.01 (0.06) nm and 2.89 (0.10) nm for subunits "A" and "B", respectively (Fig.4.2e). This indicates that the protein fluctuates close to this symmetric *open* conformation (Fig.4.1) within this time-scale (27 ns), which is more than twice the time needed for the conformational change to occur (<13 ns of MD).

CAP$^{*}_{\mathbf{aq}}$. In order to check the dependence of our results from the initial model used, we carry out an MD simulation of CAP in solution based on a different initial conformation, the symmetric *closed* conformation of CAP that is observed in the X-ray structure of the protein in complex with DNA [44] (Fig.4.1). The RMSD increases and then oscillates around a value of $\backsim$0.5 nm (Fig.4.2c). Very early in the simulation (at $\backsim$1 ns of MD), the DBD of subunit "A" reorients to the *open* conformation, and the DBD of subunit "B" undergoes a similar change within the first 10 ns. After 15 ns of MD, the distances between the mass centers of the DBD and the corresponding CNBD are 3.11 nm and 3.03 nm for subunits "A" and B, respectively (Fig.4.2f), suggesting that the protein in solution moves to the *open* conformation independently from the initial structure (Fig.4.3).

In conclusion, our simulations suggest that the DNA-free ligand bound protein

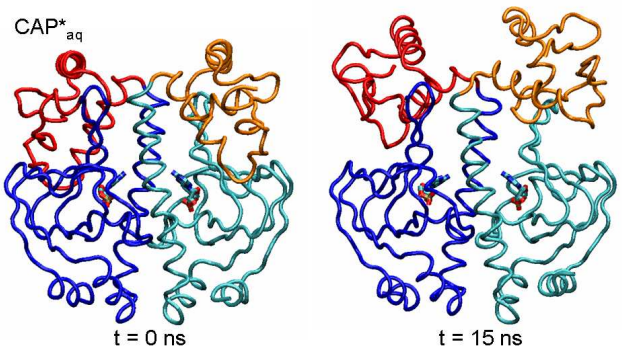

Figure 4.3: Trace representation of the structure of CAP in aqueous solution ($\mathbf{CAP}^*_{aq}$) in the initial conformation, i.e. as in the X-ray structure of the DNA-bound protein [44], and as after 15 ns of MD. The CNBD and the DBD of subunit "A" are colored in blue and red, respectively, while the same domains of subunit "B" are colored in cyan and orange, respectively; the cAMP molecules are drawn in sticks and colored by atom type. Figures obtained with the VMD program [235].

in solution assumes an *open* conformation in aqueous solution, in which both DBDs are separated from the respective CNBD by a large cleft (Fig.4.1). This result holds true independently from two, rather different, initial structures used in the simulation. Thus, the asymmetry of the experimental X-ray structure, which is reproduced by our computational setup, is possibly caused by packing contacts within the crystal environment (Fig.4.1 and Tab.4.2). Such *open* conformation could play a role for DNA binding.

Electrostatic profiles. To provide further insights on DNA molecular recognition by CAP, we carry out a comparative electrostatic analysis between the structure of the CAP bound to DNA (*closed* conformation, Fig.4.1) and our model in solution (*open* conformation, Fig.4.1).

When the protein is in the *closed* conformation, as in the DNA-bound complex [44] (Fig.4.1), the DNA binding interface of the protein is characterized by a dominant positive area, which provides electrostatic complementarity to DNA (Fig.4.4a,c). On the contrary, the electrostatic potential on the same surface of the protein in the *open* conformation (calculated here on $\mathbf{CAP}_{\mathbf{aq}}$ final MD structure, Fig.4.1) appears

qualitatively different in the proximity of the homodimeric symmetry axis, i.e. near the hinge regions (Fig.4.4b,d). Since the reorientation of the hinges is a key step in the allosteric mechanism coupling the two domains [51, 49, 23], differences in this region might play a biological role. Charged residues in this region are Asp-138 and Arg-142: in the *open* conformation, Arg-142 side chains are buried within the intersubunit region (Fig.4.4f), while in the *closed* conformation they are exposed to the DNA binding interface (Fig.4.4e). The differences in the electrostatic profiles are also due to Asp-138, which is known to play a crucial role for transmitting the allosteric signal [51]: in fact, Asp-138 are closer to the dimeric symmetry axis of the protein in the *open* conformation (Fig.4.4e,f). Thus, when the protein is in the *open* conformation, the dominant positive potential at the DNA binding interface is intercalated by a negative region in the central part of the surface (Fig.4.4b,d).

Simulation of CAP with lower water content than in CAP$_{cryst}$. 7,468 water molecules are added to the CAP in crystal condition by adding a water box with 1.0 Kg/l density. The water molecules are rejected if the distance between any solvent atom and the closest solute atom is lower than the sum of their respective van der Waals radii.

The RMSD for the whole unit cell increases during the first 5 ns and then fluctuates at $\backsim$0.24 nm, while the mean RMSD for the four asymmetric units is $\backsim$0.16 nm (Fig.4.5a). The mean distances between the mass centers of the CNBD and the DBD are 2.56 (0.06) nm (2.41 nm minimum and 2.70 nm maximum) and 2.96 (0.04) nm (2.83 nm minimum and 3.05 nm maximum) for subunits “A” and “B”, respectively (Fig.4.5b); the initial values are 2.66 nm and 2.92 nm. The calculations do not fully reproduce the X-ray unit cell parameters (a=4.68 nm, b=9.56 nm and c=10.55 nm, while the mean dimensions of the MD simulation box are 4.62 nm, 9.44 nm and 10.42 nm). Thus, the decrease of the unit cell volume is $\backsim$4%.

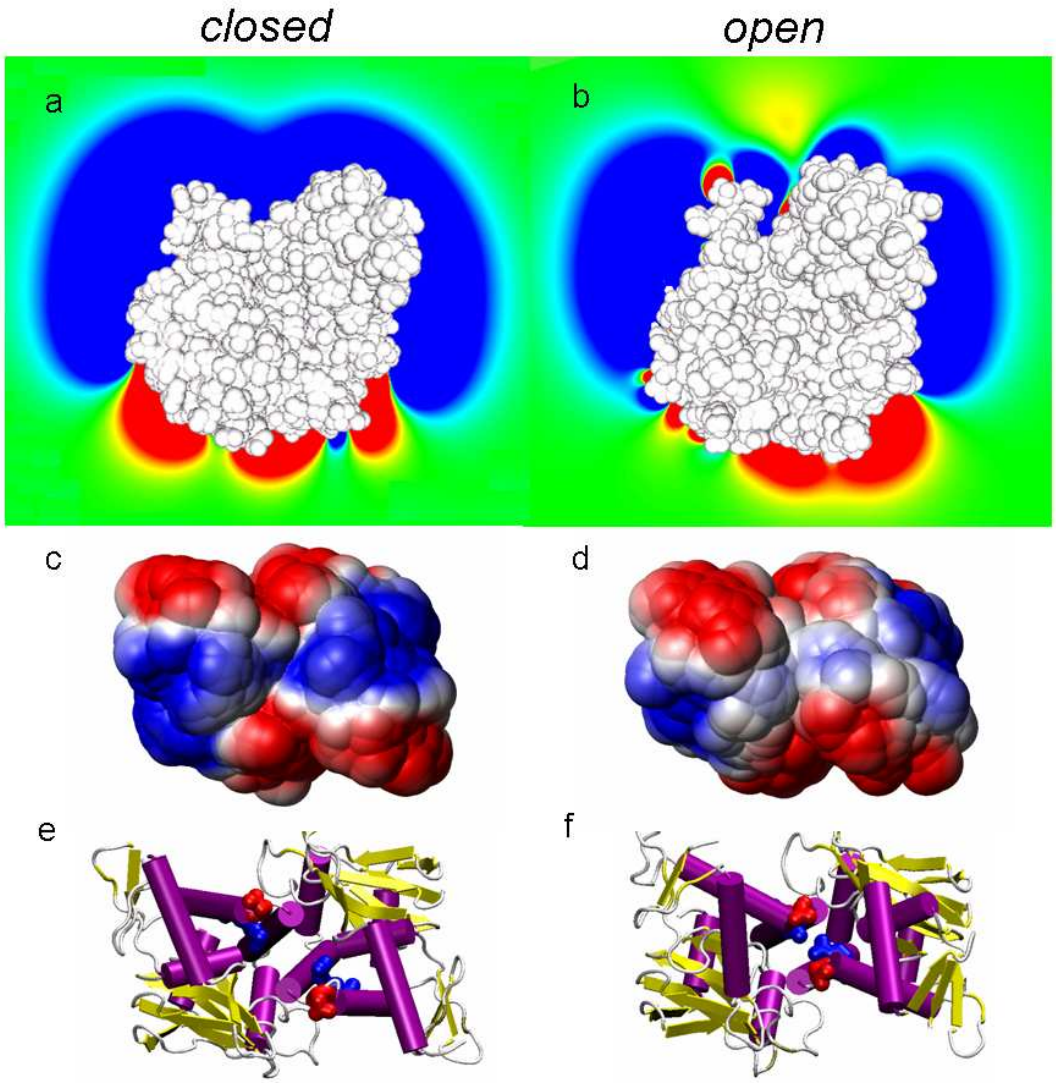

Figure 4.4: **Electrostatics properties.** (a-b) van der Waals surface (colored in white) of the protein in the *closed* (**CAP·DNA**, a) and *open* (**CAP$_{aq}$** after 40 ns of simulation, b) conformations, view as in Fig.1. The electrostatic potential is plotted on the plane defined by the positions of Cα atoms of Arg-180 from subunit "A" and "B", and by the midpoint between Pro-110 Cα atoms, and is colored in red at -125 mV and in blue at +125 mV. The pictures are obtained using the gOPENMOL program [241, 242]. (c-f) View of the protein rotated by 90° relative to (a-b), which shows the DNA-binding interface region. Both the *closed* (c,e) and *open* (d,f) states are plotted as van der Waals surface (c,d) or as cartoon (e,f). In (c,d), the electrostatic potential is plotted on the protein surface drawn by the center of a probe of radius 0.5 nm and colored in red at -20 mV and in blue for +20 mV, using the MOLMOL program [243]. In (e,f), helices are colored in violet and strands in yellow; Asp-138 and Arg-142 are drawn in sticks and colored in red and blue, respectively.

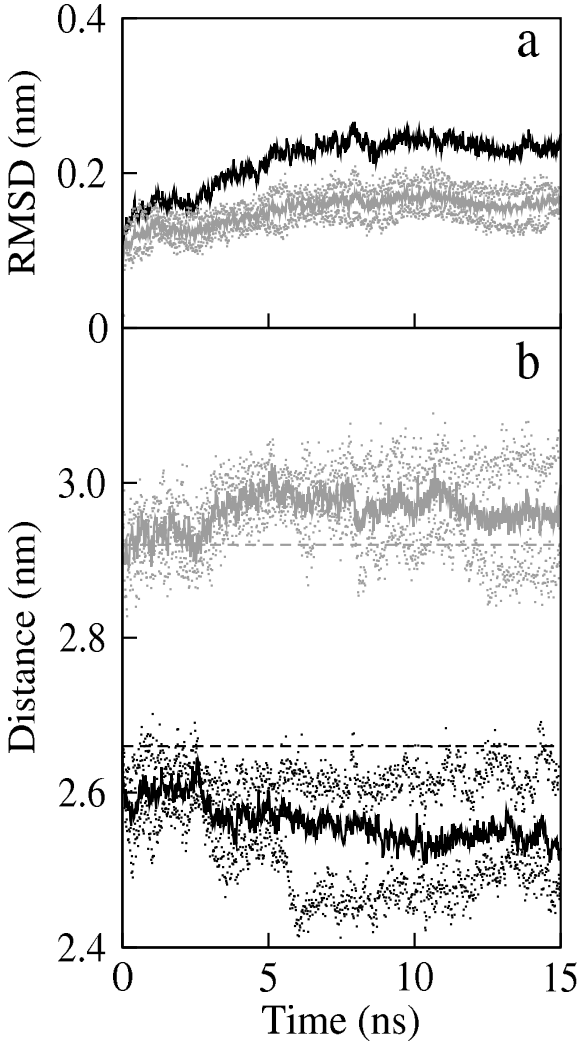

Figure 4.5: (a) RMSD are plotted as a function of the simulation time (black line). The RMSD is also averaged over the four proteins in the unit cell and extreme values are reported as dots (gray line). (b) Distances between CNBD and DBD mass centers in subunits "A" and "B" (solid and gray lines, respectively) averaged over the 4 asymmetric units of the unit cell and plotted as a function of the simulation time. Extreme values are indicated by dots and initial distances are indicated by the horizontal dashed lines.

4.3 Concluding remarks

MD simulations are used here to investigate the structural features of the cAMP-activated CAP in solution, providing complementary information that does not emerge from the available X-ray structures and are of critical importance to describe the functional mechanism of the protein [45, 56, 57].

Our calculations suggest that crystal packing contacts affects the DNA-free CAP conformation and that the ligand-activated form of CAP is the symmetric *open* conformation (Fig.4.1).

The protein conformation obtained by our MD simulations in aqueous solution (*open* conformation, Fig.4.1) differs from the conformation of the protein in the DNA-bound X-ray structure (*closed* conformation, Fig.4.1) [43, 41, 44] not only for the orientation of the DBDs, but also for the electrostatic potential at the DNA-binding interface, as the latter conformation presents a large positive region, which in the *open* conformation is interrupted in the proximity of the hinges (Fig.4.4). We speculate that this electrostatic profile may mediate a first step in DNA bending. Before the molecules get in direct contact, the positive regions of the DNA-binding interface of the protein in the *open* conformation attract the DNA, while a kink is generated in DNA segments prone to bending [33,65]. Subsequently, both macromolecules could enter in direct contact and a mutually induced-fit mechanism could drive the complex from the *open* to the *closed* conformation, which provides a larger complementary electrostatic surface for the bound DNA (Fig.4.4). Furthermore, experimental and/or theoretical studies are required to test this hypothesis.

4.4 Reference

The work reported in the present chapter will be published in the following article:
Marco Berrera, Sergio Pantano and Paolo Carloni *"Catabolite Activator Protein in aqueous solution: a molecular simulation study"* submitted.

Chapter 5

cAMP modulation of the HCN2 channel

HCN2 is the most characterized member of the hyperpolarization-activated cyclic nucleotide-modulated channels family. In this channel, CNBD inhibits channel activity by a mechanism which depends on the C-linker/CNBD interactions: binding of cAMP relieves this inhibition and shifts by $\sim$+17 mV the voltage dependence to less negative values [103, 104].

Recently, Molecular Dynamics (MD) simulations provided valuable insights in the regulation mechanisms in different ionic channels (such as the nicotinic receptor and the kir channel) under conditions that are difficult to achieve with experimental techniques [13, 14, 244, 245, 246]. Based on the available structural information [27], here we study the cytoplasmic part of HCN2 by means of MD simulations, to provide a description of the molecular process driven by cAMP leading to channel modulation.

Based on our calculations, we propose that the allosteric mechanism of cAMP modulation originates from oscillations of CNBD quaternary structure around its average structure, with a periodicity in the order of 10 ns. This large-scale breathing motion is triggered by cAMP binding: in fact, in the absence of the ligand, CNBD assumes a rather disordered and loose structure, similarly to what has been found in other CNBDs with the same fold [247, 125, 122, 46, 47] and no quaternary structure oscillations are observed.

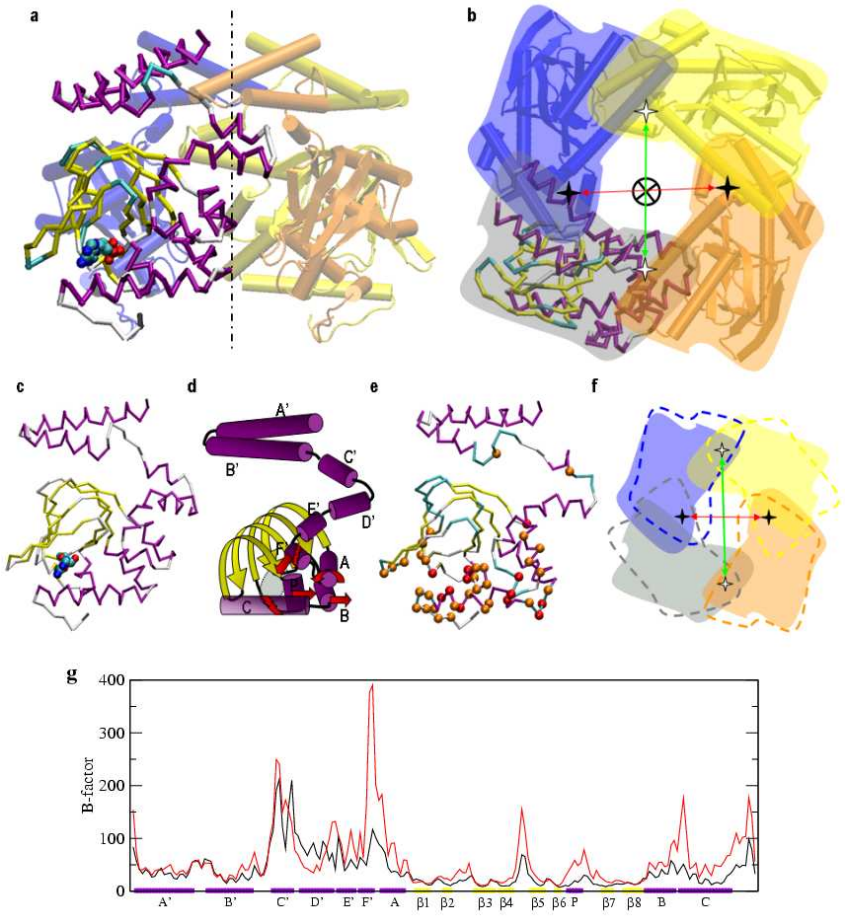

Figure 5.1: (a) Structure of C-linker and CNBD of HCN2 from mouse [27]: four subunits are arranged around the four fold rotational symmetry axis, which is represented by the dashed line, forming the homotetramer. C-linker are at the top and CNBDs at the bottom of the picture. Three subunits are drawn in cartoons and in the fourth, which is drawn in trace, secondary structure elements are colored in violet for helices and yellow for β-strands and one cAMP is shown. (b) Upper view of the complex: stars indicate mass centers of opposite couples of adjacent subunits. (c) Diagram of one subunit of HCN2 C-linker and CNBD with cAMP in its binding site. (d) Cascade of helices rearrangements following ligand unbinding [125, 122, 46, 47]. (e) Representative snapshot of the apoprotein, to be compared with *c*: balls represent residues whose B-factor in the apoprotein is at least 2 (orange) and 3 (red) times that in the holoprotein, which are spread in the CNBD and E' and F' helices, including residues forming the binding site. (f) The most relevant motions in the holoprotein are oscillations of the quaternary structure, which are here identified by the distances between mass centers of opposite couples of adjacent subunits (stars as in *b*) and are plotted in Fig.2c-d. (g) B-factors in the holoprotein (black line) and in the apoprotein (red line) are plotted along the sequence. Secondary structure elements are indicated in violet for helices and yellow for β-strands, and are labeled.

5.1 Computational details

The holoprotein is the X-ray structure of the cytoplasmic domains of HCN2 channel from mouse in complex with four equivalents of cAMP, solved at 2.30 Å resolution (residues 443 to 645, pdb entry 1Q5O [27, 22]). The protein is a homotetramer, with a four fold rotational symmetry (Fig.5.1a-b). The apoprotein is obtained by removing the four cAMPs. H atoms are added by assuming standard bond lengths and bond angles. Histidines 463, 474, 479 and 559 are protonated respectively on their Nϵ, Nδ, Nϵ and Nδ as this choice optimizes the formation of the H-bond network with their surroundings. Acid and basic residues are assumed to be ionized at the physiological conditions. The models are immersed in parallelepiped boxes whose edges are ∼10.0, 10.0 and 8.1 nm, containing ∼22,500 water molecules; 12 and 16 chlorine ions are added to neutralize the boxes.

The AMBER99 [192, 248, 193] and the TIP3P [194] force fields are used for the protein (and ions) and water respectively; parameters for cAMP are obtained from Punta et al. [236]. Rectangular periodic boundary conditions are applied. Particle mesh Ewald is used to evaluate long range electrostatics [202, 203, 201]. A cutoff of 1 nm is used for the real part of the electrostatics and van der Waals interactions. The neighbor list is updated every 10 steps. Constraints are applied to the chemical bonds using the LINCS algorithm [199]. The integration time step is set to 1.5 fs.

The GROMACS program is used [238, 197]. After energy minimization, 45 ps of MD of the solvent and a gradual heating of the systems (8 runs, 22.5 ps each, from 0 to 10, 30, 70, 100, 150, 200, 250, 300 K, using the Berendsen thermostat and barostat [204]), the complexes undergo 2.3 ns of MD in the NPT ensemble at 300 K and 1 atm pressure, using the Nosé-Hoover thermostat [206, 237] and the Parrinello-Rahman barostat [207, 205]; the pressure coupling is isotropic in all directions. After about 2 ns, the average RMSD for single subunits fluctuates around 0.15 nm in both systems (Fig.5.2a-b). Finally, 19.7 ns MDs are performed in the NVT ensemble, using the Nosé-Hoover thermostat [206, 237].

The following properties are calculated: (i) Root Mean Square Deviations (RMSD)

are calculated respect to the X-ray structure [238, 197]. (ii) B-factors are calculated after fitting the four subunits to the starting conformation of one monomer [238, 197]. (iii) Essential Modes (EM) are obtained diagonalizing the covariance matrix [249, 226, 239, 225, 224, 238, 197]: cosine contents are calculated for the first 10 eigenvectors [227, 228, 238, 197]. (iv) Intersubunit contact surface is evaluated as the difference between solvent accessible surface areas [220, 221, 238, 197] calculated for isolated subunits and for the tetramer. (v) The secondary structure elements are identified by the DSSP program [250]. Properties i-iii are calculated considering only Cα and properties ii-iv are calculated for the last 20 ns of MD.

To complement the study of the protein dynamic properties, we perform elastic network analysis by applying a modified version of the Gaussian model, which consider also the Cβ atoms [9].

5.2 Results and discussion

5.2.1 Holoprotein

During the MD simulation, the RMSD of the ligand bound protein increases up to nearly 0.2 nm within the first 2 ns; subsequently, the RMSD fluctuates between 0.2 and 0.3 nm (Fig.5.2a), with an overall oscillation in the ∼13 ns time-scale. Also the distances between centers of mass of two complex halves (Fig.5.1b,f), which are perpendicular to the homotetramer rotational symmetry, oscillate with the same period and an amplitude of about 0.05 nm (Fig.5.2c and Fig.5.1b,f). The protein oscillates between a configuration similar to that of the X-ray structure and a conformation where two opposite intersubunit interface regions are more distant than the other two. The projection of the first Essential Mode (EM) on the real space trajectory reproduces this movement (Fig.5.3 and animation available at http://www.sissa.it/∼berrera/HCN2/movies.html). The corresponding eigenvalue accounts for about 24% of the total fluctuations. No large intrasubunit rearrangements are observed and the RMSD of single subunit is nearly 0.15 nm (Fig.5.2a). The cosine contents of the first 10 EMs are as small as 0.2, indicating that the simulation is rather converged [227, 228]. A Gaussian elastic network model [9] calculation provides a similar picture: the two slowest normal modes de-

scribe conformational motions which evolve perpendicularly to the homotetramer axis (animation at the address above), similarly to what obtained from the EM analysis of the MD trajectory. The scalar product of the first EM with the first and the second β-Gaussian normal modes are 0.5 both, and the subspace overlap of the first EM with the first 10 β-Gaussian normal modes is 0.82, meaning that the first EM is well described in the vibrations of the elastic network model. Moreover, the eigenvalues of the first 10 EMs, which account for about 70% of the total fluctuations, correlate with the corresponding eigenvalues of the β-Gaussian normal modes (Fig.5.4). In addition, the secondary structure elements and the protein/ligand contacts observed in the X-ray structure are fully maintained throughout the MD trajectory.

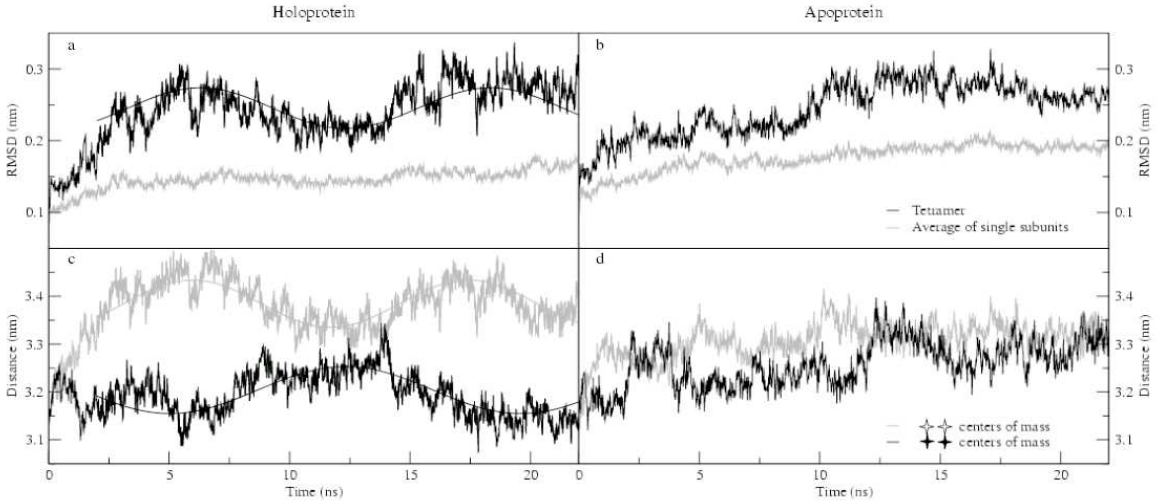

Figure 5.2: Cα RMSD plots (a-b) and distances between mass centers of opposite couples of adjacent subunits (c-d) according to Fig.1b and f, in the holoprotein (a and c) and in the apoprotein (b and d). RMSD for the tetramer (black) and average RMSD for single chains (gray) are shown. For the holoprotein, distances and RMSD plots are correlated and display an oscillation that can be fitted by a sine function with an period of ∼13 ns and an amplitude of ∼0.03 nm for RMSD and ∼0.05 nm for both centers of mass distances.

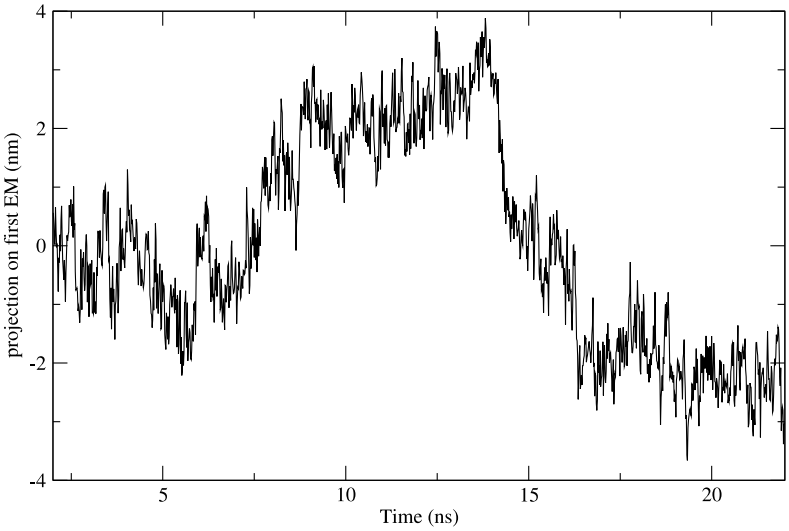

Figure 5.3: Projection on the first Essential Mode (EM) calculated from the holoprotein's MD trajectory, as a function of the simulation time.

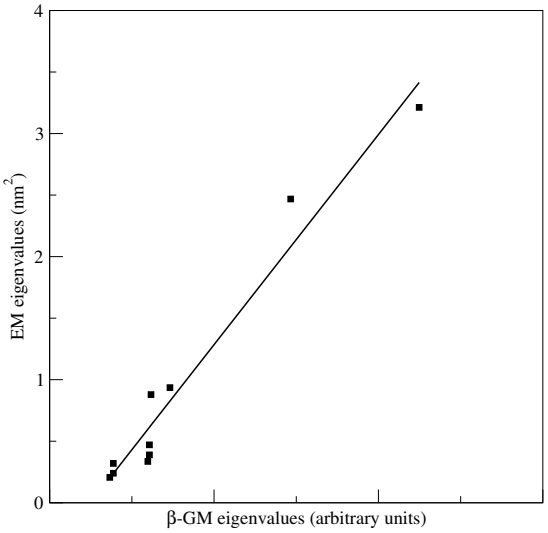

Figure 5.4: Eigenvalues of the first 10 EMs calculated from the MD simulation of the holoprotein ($\simeq$70% of the total fluctuations) are plotted against the corresponding eigenvalues of the β-Gaussian normal modes. The correlation coefficient is about 0.98.

5.2.2 Apoprotein

Also the RMSD of the ligand free protein increases up to nearly 0.2 nm within the first 2 ns, and subsequently fluctuates between 0.2 and 0.3 nm without the oscillation identified above (Fig.5.2b). A plot of the distances between the same centers of mass defined above confirms that the quaternary structure does not oscillate as in the cAMP bound system (Fig.5.2d). In addition, the motion of each subunit is uncorrelated to that of the others. The RMSDs of each subunit fluctuate around 0.2 nm toward the end of the simulation (Fig.5.2b), suggesting that in this case fluctuations within single chains are more relevant. In fact, the absence of the ligand causes a cascade of dramatic rearrangements first affecting C- and P-helices, which are elements forming the binding pocket. These rearrangements have been already observed in CNBDs of other proteins with the same fold [247, 125, 236, 122, 46, 47] and are here only briefly summarized (Fig.5.1d). The C helix breaks, increasing the flexibility of its extremities. This allows for a rotation of the P-helix around its longitudinal axis as observed in other CNBDs [125, 122, 47]. The movements of the C- and P-helices are also transferred to B-, A- and F'-helices, this last within the C-term part of the C-linker. F'-helix moves closer to C-helix of CNBD and its secondary structure breaks. These rearrangements are linked to residues bearing higher flexibility, as evidenced by a comparison of the B-factors in the apoprotein with those of the holoprotein (Fig.5.1e,g). The cosine content of the largest EM is 0.8 and those of the following 9 are as small as 0.2, probably suggesting that the system has not reached yet a fully converged state.

Finally, the intersubunit interaction appears to be stronger in the apoprotein than in the holoprotein, because the intersubunit contact surface is respectively 74 (2) nm^2 and 69 (2) nm^2 [251], compatible with the fact that, in the holoprotein, the subunits undergo large oscillations one relative to the others.

5.3 Concluding remarks

Protein fluctuations play a crucial role for a large variety of protein functions [252, 253]. In this work, we have shown that MD simulations provide complementary and important information not emerging from the X-ray structure of the complex between the cytoplasmic domains of HCN2 and cAMP. In fact, the motion of the holoprotein is characterized by quaternary structure oscillation, hinged at the intersubunit contact surface: two opposite edges of the complex go far and closer with a period of about 13 ns (Fig.5.1f, Fig.5.2c and animation at the address above). Elastic network analysis supports these conclusions.

A reduction of the intersubunit interactions due to electrostatics has been proposed to facilitate the opening transition of the C-linker [254, 255]. Thus, at the speculative level, we propose that also the weakening of the van der Waals interactions can play a role for gating. In fact, our calculations indicate that the cAMP binding induces a reduction in the contact surfaces between subunits, i.e. it leads to a weakening of the intersubunit van der Waals interaction.

The MD simulations provide also insights on the cytoplasmic domains in the ligand free form, for which no structural information is available. CNBD experiences a cascade of rearrangements of secondary structure elements: the repositioning of P-helix and the increased flexibility of C-helix lead to a reorientation of B-helix, which in turn affects A helix and the C-terminal part of C-linker (Fig.5.1d). Very similar cascades of events have been seen previously in the context of CNBDs with the same fold in different proteins [47], pointing to a ligand-dependent orientation of C-helix relative to the β-roll [247, 236, 46] and to a conformational change in the PBC following ligand release coupled to a reorientation of the B-helix by hydrophobic residues, which are conserved in CNBDs from different proteins and corresponds in HCN2 to LEU585 of P helix and PHE611 of B-helix [125, 122, 46]. In fact, in the apoprotein a rotation of the P-helix turns LEU585 side chain to push PHE611 side chain.

In conclusion, MD simulations allow us to dissect important aspects of the mechanism for cAMP allosteric modulation in the HCN2 channel. We must note that the

structural features reported here for the cAMP free and bound systems are confined to the relatively short time-scale allowed by the state-of-the-art simulation techniques. Nevertheless, our results are in agreement with a variety of experimental data present in the literature and allow to formulate a molecular level model for the cAMP modulation of the HCN2 channel.

5.4 Reference

The work reported in the present chapter has been published in the following article: Marco Berrera, Sergio Pantano and Paolo Carloni. *"cAMP modulation of the cytoplasmic domain in the HCN2 channel investigated by molecular simulations"* Biophysical Journal (2006) 90:3428-3433.

Chapter 6

Binding of NGF peptide mimics to trkA

NGF binds with the highest affinity to the receptor trkA [136, 137, 138], which mediates the survival-promoting and neurite-growth-promoting effects of NGF during development [139, 140, 141, 142]. The ligand/receptor interface involves two patches: one comprises residues of NGF core region and loops of the C-term of the fifth extracellular domain of trkA (trkA-d5), the other includes the N-terminal fragment of NGF (N-term@NGF) and the 'ABED' β-sheet of trkA-d5 [157, 28] (Fig.6.1a). The latter is known to determine the affinity and specificity of the NGF binding to trkA, as indicated by experimental data [158, 159, 160, 161, 162, 164, 141] and further suggested by Molecular Dynamics (MD) calculations [165].

Here we attempt at identifying a short peptide as a trkA-d5 high affinity mimic of the N-term@NGF. Our work is based on the X-ray [28] and the MD [165] structures of the NGF/trkA-d5 complex (Fig.6.1a). First, we identify NGF residues exhibiting significant contact surface, and thus non-polar interaction, with the receptor; among those, we locate the residues forming significant electrostatic interaction and/or binding energy hot spot as defined in ref. [190, 191]. Based on this analysis, we conclude that residues from 4 to 13 (*H4PIFHRGEFS13*, according to the pdb 1WWW numeration [28, 22]), at the N-term, may have high affinity for trkA-d5.

Subsequently, under the assumption that the mode of binding of the peptide is similar to that of the original protein, we investigate the conformational flexibility of the adduct formed by the *H4PIFHRGEFS13* peptide with trkA-d5 using MD (Fig.6.1b).

The stability of the "complementary" complex, i.e. the complex in which the same peptide is removed from NGF, is also explored by MD (Fig.6.1d). Our calculations confirm that most residues belonging to the 4-13 peptide are important for trkA-d5 binding, HIS8 and SER13 being the only groups not stabilizing the complex. Thus, we modify the peptide mimic by deleting SER13 and mutating HIS8 to GLY, which ensures a larger flexibility of the peptide. MD simulations carried out on the resulting peptide (*H4PIFGRGEF12*) suggest that the latter, in spite of its shorter length, forms an additional salt bridge with the receptor, besides those originally formed by ARG9 and GLU11. Thus, we identify this peptide as a high affinity mimic of the N-term@NGF. As a final step, we investigate the binding process by steered MD [211,212,213,217,214, 215, 216, 218, 219], and the aforementioned salt bridges turn to be the most persistent interactions between the ligand and the receptor.

6.1 Computational details

6.1.1 Features of the N-term@NGF / trkA-d5 interactions

All the calculations presented here are based on the last snapshot (available at http://www.sissa.it/∼berrera/NGF/NGF-trkAd5-t0.pdb) of our MD simulation of the NGF/trkA-d5 complex [165]. Calculations based on the X-ray structure [28] yield very similar results (Tab.6.2).

We focus on structural (i) and energetic (ii-iii) features associated with the binding of chain Y of trkA-d5 to NGF homodimer in complex with the other receptor chain X:

$trkA{-}d5(Y) + NGF \cdot trkA{-}d5(X) \rightarrow trkA{-}d5(Y){\cdot}NGF \cdot trkA{-}d5(X)$

(i) We calculate the difference of the solvent accessible surfaces of NGF in the presence and in the absence of trkA-d5(Y), which is here called Contact Surface (CS). CS provides a rough estimate of the non-polar contribution to the binding free energy [223]. We use the center-probe area definition [220] and set the solvent probe radius to 0.14 nm [221, 222]. The residues providing the largest CS in the NGF N-term region turn out to be located between HIS4 and SER13 (sequence H4PIFHRGEFS13).

(ii) The Poisson-Boltzmann Equation (PBE) [189] is applied to calculate the electrostatic contribution to the free energy of binding ΔG_B^E [256]:

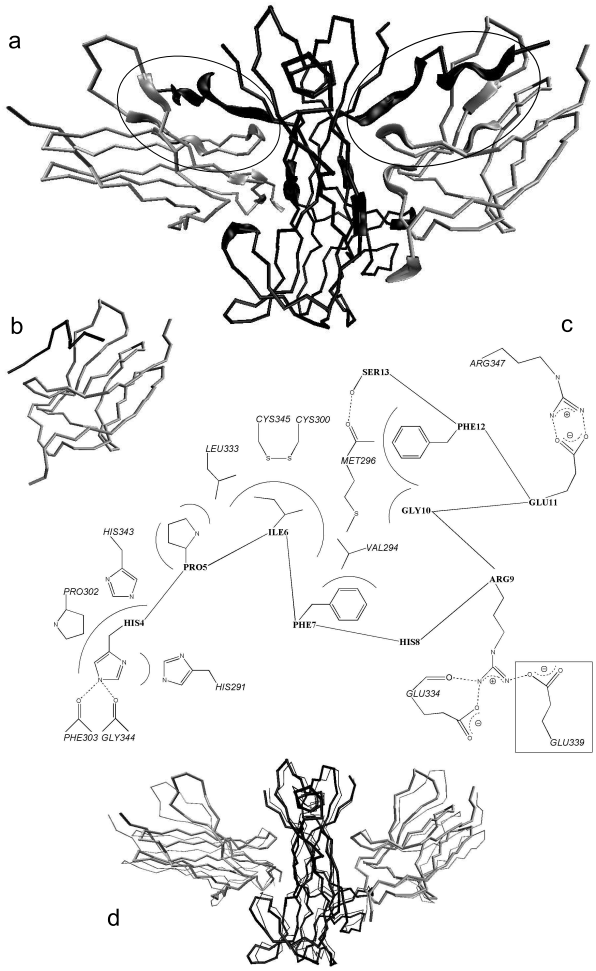

Figure 6.1: (a) Cα trace of the NGF/trkA-d5 complex as obtained by the MD simulation of ref. [165]. Each of the two NGF identical subunits (black) binds to a trkA-d5 subunit (gray). The trace is thicker for the residues involved in NGF/trkA-d5 molecular recognition. The trkA-d5/N-term@NGF regions are further marked with two ellipses. (b) Cα trace of the complex formed by trkA-d5 and *H4PIFHRGEFS13* (**c1**). A second peptide in **c2** differs from that in **c1** for the replacement of HIS8 with GLY and the removal of SER13. Both **c1** and **c2** are investigated here by MD simulations. (c) TrkA-d5/peptide interactions in **c1** and **c2**. The van der Waals and H-bond interactions are depicted as continuous and dashed lines respectively. HIS4 is accommodated in a receptor's pocket lined by HIS291, PRO302 and HIS343; at the bottom, HIS4 hydrogen bonds with PHE303 and GLY344. PRO5 side chain interacts with HIS343 and LEU333. ILE6 is positioned in another receptor's pocket lined by VAL294, MET296 and LEU333; at the bottom, ILE6 side chain forms van der Waals interactions with the receptor surface exposed disulfide region between CYS345 and CYS300. PHE7 interacts with VAL294, ARG9 with GLU334, GLY10 with MET296, GLU11 with ARG347, PHE12 with MET296, SER13 with MET296. HIS8 does not interact with trkA-d5. GLU339, which is boxed, interacts with ARG9 only in **c2**. (d) Cα trace of the trkA-d5/NGF complex *without S2SHPIFHRGEFS13* residues (**c3**). Also this complex undergoes MD simulation. The initial structure (thick trace) is compared with the last **c3** MD snapshot (thin trace) [235].

$$\Delta G_B^E = G^E_{trkA-d5(Y)\cdot NGF\cdot trkA-d5(X)} - G^E_{NGF\cdot trkA-d5(X)} - G^E_{trkA-d5(Y)}$$

Each molecule is assumed to adopt the same conformation in the complex and in the isolated form. Then, the change of ΔG_B^E upon mutation of each residue R (except GLY) to ALA is calculated from the formula:

$$\Delta\Delta G_B^E = \Delta G_B^E(R \rightarrow ALA) - \Delta G_B^E(WT)$$

The structures of the mutated protein are obtained by deleting all the side chain atoms of residue R except the Cβ, which is saturated. Then, the structures undergo an energy minimization, using the standard pairwise generalized Born/surface area model of solvation [208, 209] as implemented in the AMBER7 program [257]. We use the AMBER99 force field [192, 193], assuming 100 mM monovalent ionic concentration, protein dielectric constant $\epsilon_{in} = 2$ and solvent dielectric constant $\epsilon_{wat} = 78.5$.

ΔG_B^E is calculated using the APBS program [232] under the following conditions: (i) the nonlinear PBE is solved; (ii) the temperature is set to 300 K; (iii) a 100 mM monovalent ion concentration is assumed; (iv) the Connolly molecular surface definition [258] is used; (v) a 2 runs focusing procedure is applied. First, we run the APBS program with boundary conditions defined using a Debye-Hückel model for multiple charged spheres, along with a grid spacing of 0.067 nm. Then, we run the program with boundary conditions derived from the first run, with grid spacing as small as 0.047 nm. Test calculation with a finer grid spacing, i.e. 0.045 nm, shows that the calculated free energies differ by $\backsim$0.2 kJ/mol ($\simeq$0.1 kT).

(iii) We calculate which NGF residues at the NGF/trkA-d5(Y) interface contribute significantly to the complex stability using Baker's computational alanine scanning procedure [190, 191]. The predictor locates the residues at the interface which significantly destabilize the complex when mutated to alanine, estimating both the van der Waals and the electrostatic contributions to the free energy of binding. Binding energy hot spots are defined as residues whose $\Delta\Delta G_B^{hs} \geq 2kT$. The prediction is performed on the entire NGF/trkA-d5 and on the N-term@NGF mimic/trkA-d5 complexes.

6.1.2 Molecular dynamics

We perform MD simulations on: (i) the complex formed by trkA-d5 and the N-

term@NGF derived peptide *H4PIFHRGEFS13* (**c1**, Fig.6.1b). HIS4 and SER13 are terminated by acetyl and N-methyl groups respectively. (ii) the trkA-d5/NGF complex without such peptide, along with SER2 and SER3 (**c3**, Fig.6.1d). (iii) The complex formed by trkA-d5 and the peptide of sequence *H4PIFGRGEF12* (**c2**). **c1**, **c2** and **c3** are solvated in rectangular water boxes (Tab.6.1).

The same computational protocol is used for **c1**, **c2** and **c3.** We use the AMBER99 force field [192, 193] and TIP3P [194] for the biomolecules and water, respectively. Calculations are performed using the GROMACS program [197]. Periodic boundary conditions are applied. Particle mesh Ewald is used to evaluate long range electrostatics [202, 203, 201]. A cutoff of 1 nm is used for the real part of the electrostatics and for the van der Waals interactions. Constraints are applied to the bonds using the LINCS algorithm [199]. The integration time step is set to 1.5 fs.

Equilibration runs are carried out using the Berendsen thermostat and barostat [204]. The solvent undergoes ∼50 ps of MD simulations keeping fixed the protein atoms, in order to achieve the correct solvent density. Subsequently, the systems are energy minimized and then gradually heated by 8 MD runs with increasing temperature (22.5 ps each, from 0 to 10, 30, 70, 100, 150, 200, 250, 300 K). 5.7 ns MD simulations in the NPT ensemble (T=300 K and P=1 atm) are then performed using the Nosé-Hoover thermostat [206, 237] and the Parrinello-Rahman procedure [207, 205]; the pressure coupling is isotropic in all directions.

Root Mean Square Deviations (RMSD) are calculated for Cα atoms using the X-ray structure [28] as the reference conformation. RMSD plots for **c1** and **c2** fluctuate around 0.15 nm within the first 0.6 ns, which are discarded; on the contrary, the same plot calculated for **c3** displays increasing RMSD (Fig.6.2). The maximal distance allowed for the existence of an H-bond between hydrogen and acceptor atom is 0.25 nm, while the maximal supplement of the donor-hydrogen-acceptor angle is 60°, 0° corresponding to the extended conformation. Two oppositely charged residues are assumed to form a salt bridge interaction when at least one H-bond can be detected between their side chains.

6.1.3 Steered molecular dynamics

3 ns of Steered Molecular Dynamics (SMD) [211, 212, 213, 214, 215, 216, 217, 218, 219] are carried out in the NPT ensemble with the same setup, based on the **c2** MD last snapshot, except that the peptide is harmonically restrained (force constant is 1,000 $kJ/(mol \cdot nm^2)$ [211,217,215,219]). The restraint is initially applied at the peptide mass center and moves away from the receptor mass center with a velocity of 0.5 nm/ns. An additional 4 ns long SMD simulation is performed with the same setup but 0.25 nm/ns restraint point velocity. Then, 5.4 ns of MD in the NPT ensemble, with the same setup as above, are performed. Finally, the unbound peptide is immersed in a smaller water box (**up** in Tab.6.1) and 25 ns of MD simulation in the NPT ensemble are performed.

Complex name	amino acids	N-methyl groups	Acetyl groups	water molecules	Sodium ions	Box edges (nm) x	y	z
c1	111	2	2	9689	4	7.6	7.2	5.8
c2	110	2	2	9538	4	7.3	7.2	6.3
c3	407	4	4	24165	2	12.8	9.5	6.7
up	9	1	1	2987	0	5.1	4.3	4.2

Table 6.1: Selected features of the three complexes (**c1**, **c2** and **c3**, see also Fig.1b,d) and of the unbound peptide (**up**) systems investigated in this work.

6.2 Results and discussion

A calculation of the Contact Surface (CS) [220] between trkA-d5 and NGF suggests that the NGF residues from HIS4 to SER13 form significant contacts with the receptor ($CS > 0.20$ nm^2), except HIS8 and GLY10. In particular, HIS4 and ILE6 form the most extensive contacts with the receptor, being accommodated in specific pockets (Fig.6.1c and Tab.6.2). Based on a solvent accessible surfaces calculation, CS-based methods provide a rough estimate of the non-polar interaction [223] and thus of the residues which are responsible for the most relevant hydrophobic contributions to the overall free energy of binding. Only a few other NGF residues have such significant CS: SER19, TRP21, TYR52, PHE54, ARG59, ILE145, LYS146, GLY147, THR197,

HIS198, ARG217 and VAL225. This indicates again the relevance of the N-term@NGF for ligand/receptor interaction [158, 159, 160, 161, 162, 164, 141, 165].

To dissect the most important electrostatic interactions between N-term@NGF and trkA-d5, we perform electrostatic alanine scanning calculations [256]. We calculate the electrostatic free energy of receptor binding to the ligand in which the residue R is mutated to ALA and then we subtract the corresponding free energy calculated for the native peptide. The larger is the resulting $\Delta\Delta G_B^E$, the greater is the electrostatic contribution of residue R side chain to the binding free energy. Here we distinguish H-bonds from salt bridges, which are characterized by a larger desolvation penalty upon formation and by a much stronger electrostatic attraction, involving two oppositely charged groups [259]. HIS4, ARG9 and GLU11 turn out to provide the most negative electrostatic free energies, presumably because of H-bond and salt bridge interactions with the receptor (namely, with residues PHE303 and GLY344, GLU334, ARG347, Fig.6.1c and Tab.6.2). A similar picture is obtained by applying the Baker et al. binding energy hot spot predictor [190, 191]: within the N-term region, HIS4, ILE6, ARG9, GLU11 and PHE12 significantly contribute to the complex stability ($\Delta\Delta G_B^{hs} \geqslant 2kT$, Tab.6.2).

We conclude that NGF residues from HIS4 to SER13 have good affinity for trkA-d5, with the exception of HIS8. Thus, we may expect that the peptide which has the same sequence (*H4PIFHRGEFS13*) might have good affinity for the receptor. To investigate the stability of this peptide with trkA-d5 (**c1**, Fig1b), we perform an MD simulation along with a complementary system, which comprises both receptors trkA-d5 and the whole NGF without the N-terms (**c3**, Fig.6.1d). As for the peptide, we assume that its mode of binding is similar to that of full length NGF.

The results of the simulation of **c1** are summarized in Fig.6.2 and in Tab.6.3. The RMSD fluctuates around a relatively small value (0.15 nm, Fig.6.2) and the peptide/receptor contacts are maintained as in the full complex, with the notable exception of SER13: this residue is much more solvated here than in the full complex (Tab.6.2 and 6.3) and it is not interacting with trkA-d5 as in the full complex. Our calculations

NGF	CS (nm^2)				$\Delta\Delta G_B^E$ (kT)	$\Delta\Delta G_B^{hs}$ (kT)			
residues	1WWW	f. c.	**c1**	**c2**	f. c.	1WWW	f. c.	**c1**	**c2**
HIS4	1.03	1.06	1.00	1.19	2.99	5.40	4.60	5.18	3.44
PRO5	0.47	0.51	0.57	0.36	1.47	/	/	/	/
ILE6	0.79	0.83	0.95	0.72	-0.55	2.10	2.06	2.95	2.47
PHE7	0.39	0.49	0.54	0.25	-0.84	1.27	/	1.44	1.39
HIS8*(GLY)*	0	0	0	*0*	0	/	0.49	/	/
ARG9	0.44	0.57	0.53	1.06	2.52	0.29	2.11	2.06	2.99
GLY10	0.02	0.08	0.04	0.07	/	/	/	/	/
GLU11	0.65	0.68	0.90	0.83	6.33	0.69	2.50	1.83	2.82
PHE12	0.30	0.29	0.45	0.38	-0.22	0.70	4.18	0.70	1.93
SER13	0.34	0.39	0.10	#	-2.13	0.35	0.35	-0.22	#

Table 6.2: TrkA-d5/N-term@NGF interactions. Contact Surface (CS) [220], electrostatic alanine scanning calculations ($\Delta\Delta G_B^E$) [256] and binding energy hot spot predictions ($\Delta\Delta G_B^{hs}$) [190, 191] are reported for NGF residues from HIS4 to SER13. The NGF/trkA-d5 full complex (f. c.) is the last MD snapshot of the previously performed simulation [165] and the **c1** and **c2** conformations are those after 5.7 ns of MD.

further confirm that HIS8 does not form interactions with the receptor. This suggests that HIS8 can be substituted by a simpler residue like GLY or ALA. Since GLY allows for a higher flexibility of the peptide, which in turn might assist trkA-d5 binding, we substitute here HIS8 with GLY.

Based on these findings, we probe the stability of the peptide in which HIS8 is mutated to GLY and SER13 is absent (*H4PIFGRGEF12*, **c2**). This peptide is expected to interact with the receptor as strongly as *H4PIFHRGEFS13*, being one amino acid shorter. The peptide interacts with trkA-d5 as in **c1**, except ARG9@NGF: the salt bridge formed by this residue with GLU334@trkA is almost always broken and the H-bond formed with the backbone of GLU334@trkA is strengthened. Moreover, a new salt bridge, not present in **c1**, is observed between ARG9@NGF and GLU339@trkA but only in 40% of the trajectory (Fig.6.1c and Tab.6.3): this interaction is therefore weaker than the salt bridge between ARG9@NGF and GLU334@trkA in c1 (84%). However, it is compensated by the formation of an H-bond between ARG9@NGF and GLU334@trkA backbone (Tab.6.3). Both terminal residues are forming significant interaction with the receptor, unlike in **c1**. The complex is stable, with the RMSD fluctuating around 0.15 nm (Fig.6.2). The Baker's binding energy hot spots predic-

tor [190,191], applied to the last **c2** snapshot, suggests that all of the peptide residues, except PRO5, GLY8 and GLY10, are significantly contributing to the complex stability (Tab.6.2). We conclude that the larger conformational flexibility of the peptide caused by the HIS8 to GLY mutation might assist the formation of a new salt bridge interaction.

NGF	trkA-d5	**c1**	**c2**
H-bonds (%)			
HIS 4 N_ϵ	PHE 303 O	87	99
HIS 4 N_ϵ	GLY 344 O	22	3
ARG 9 sc	GLU 334 O	4	72
Salt bridges (%)			
ARG 9 sc	GLU 334 sc	84	1
ARG 9 sc	GLU 339 sc	0	40
GLU 11 sc	ARG 347 sc	100	100
hydrophobic contacts (nm)			
HIS4	PHE303	0.29 (0.02)	0.28 (0.01)
HIS4	GLY344	0.33 (0.04)	0.35 (0.03)
HIS4	HIS291	0.48 (0.13)	0.38 (0.04)
HIS4	PRO302	0.36 (0.02)	0.36 (0.02)
HIS4	HIS343	0.37 (0.03)	0.38 (0.03)
PRO5	HIS343	0.36 (0.02)	0.36 (0.02)
PRO5	LEU333	0.40 (0.03)	0.40 (0.04)
ILE6	LEU333	0.40 (0.05)	0.38 (0.03)
ILE6	CYS345	0.38 (0.03)	0.38 (0.03)
ILE6	CYS300	0.41 (0.04)	0.44 (0.04)
ILE6	MET296	0.35 (0.03)	0.41 (0.05)
ILE6	VAL294	0.40 (0.04)	0.47 (0.05)
PHE7	VAL294	0.43 (0.08)	0.41 (0.05)
ARG9	GLU334	0.29 (0.05)	0.33 (0.10)
ARG9	GLU339	1.14 (0.21)	0.45 (0.21)
GLY10	MET296	0.44 (0.06)	0.63 (0.10)
GLU11	ARG347	0.27 (0.01)	0.27 (0.01)
PHE12	MET296	0.34 (0.02)	0.37 (0.04)
SER13	MET296	0.42 (0.09)	#

Table 6.3: Ligand-receptor interactions in **c1** and **c2** (sc = side chain). H-bonds, salt bridges and minimum distances between non-hydrogen atoms of couples of interacting residues, as described in Fig.1c.

Very different results are obtained for the complex between trkA-d5 and the NGF lacking the N-term segments (**c3** in Fig.6.1d). In this case, although we start from the

bound conformation of the full complex, the receptor slowly detaches from the N-terms deleted neurotrophin, as evinced from the RMSD that grows during the simulation and the CS between NGF homodimer and the receptors that decreases, indicating an increase of the solvation of the different subunits during the dynamics (Fig.6.1d and Fig.6.2). The calculation is stopped after 5.7 ns of MD, as the previously described simulations. Although the results strongly suggest a dissociation of the complex, observing such an event requires a time-scale which is currently not covered by MD simulations.

We conclude that the interactions of the peptide in **c2** with the receptor appear to be far stronger than those formed by the rest of the neurotrophin.

6.2.1 Steered molecular dynamics

SMD is based on the final MD snapshot of **c2** (Fig.6.3b). Although the investigation of the entire molecular recognition process is beyond the domain of applicability of molecular simulation methods, useful qualitative insights on the ligand/receptor binding process can be obtained by steering the ligand away from the receptor and observing the applied force profile [211, 212, 213, 214, 217, 215, 216, 218, 219].

Here we apply such an approach to the case of **c2,** by monitoring the external force and the distance between the mass centers of ligand and receptor as a function of the simulated time (Fig.6.3a). Until 0.8 ns the distance is almost constant, no ligand/receptor interactions are broken and the force grows linearly as fast as 1.12 pN/ps. Then, at about 1 ns, the force is large enough to break almost simultaneously all intermolecular interactions except the salt bridges formed by ARG9@NGF and GLU11@NGF. The breaking of all these interactions determines a sharp decrease of the force, an increase of the receptor/peptide mass centers distance and of the solvation of the NGF residues (Fig.6.3a). The force is now much smaller and does not change on the disruption, at about 1.45 ns, of the salt bridge formed by ARG9, which is observed in **c1** and in **c2** to be the least stable among the two peptide/receptor salt bridges (Tab.6.3). In contrast, it decreases suddenly on the rupture of the last interaction, the salt bridge formed by GLU11, at about 2.15 ns (Fig.6.3a). The hydration

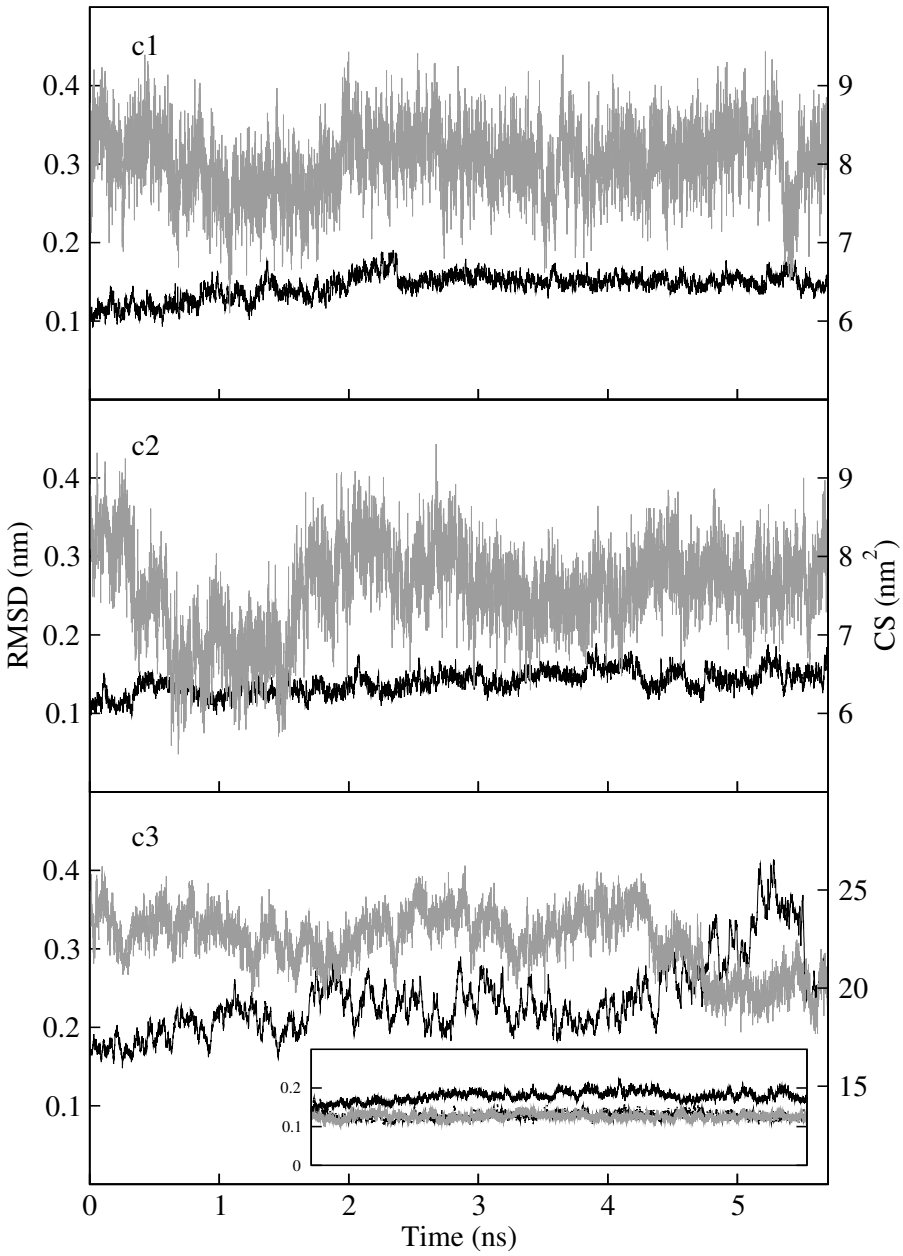

Figure 6.2: RMSDs (black line) and CS between ligand and the receptor (gray line) calculated for the three complexes investigated here by MD. The insert shows the RMSDs of NGF and trkA-d5 chains X and Y in **c3** (continuous black line, dashed black line and continuous gray lines, respectively).

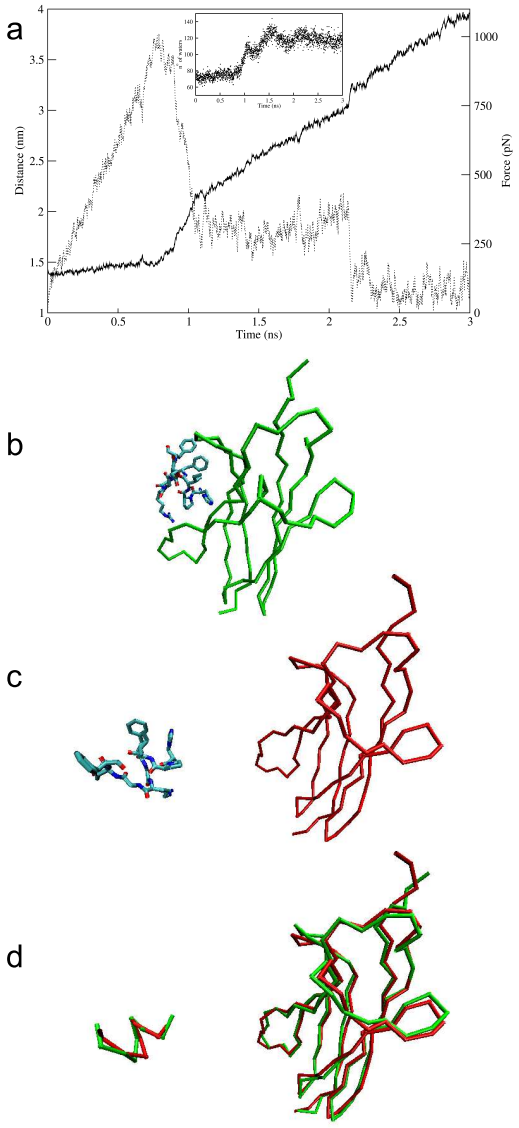

Figure 6.3: SMD of **c2** moving the restraint point with a velocity of 0.5 nm/ns. (a) Distance between the mass centers of trkA-d5 and of the ACE*HPIFGRGEF*NME peptide (solid line) and force on the peptide (dashed line) plotted as a function of the simulation time**.** The peptide/receptor interactions are broken after 1.1 ns of SMD, except the salt bridges formed by the peptide residues ARG9 and GLU11, which break down at about 1.45 ns and 2.15 ns of SMD respectively. The insert shows the number of water oxygens within 0.45 nm of non-hydrogen atoms of the peptide residues, as a function of the simulation time. (b-c) Structure of **c2** at the beginning (b) and at the end (c) of the simulation: the Cα trace of the receptor is represented (green at 5.7 ns of MD, red after 3 ns of SMD and further 5.4 ns of MD), along with the sticks representation of the peptide, colored by atom type. (d) Separated fit of the peptide and of the receptor structures in the initial (green) and the final (red) conformations [235].

of the ligand increases at each of these disruptive events (insert in Fig.6.3a).

To check the reliability of our results, a second SMD simulation is performed by applying an external force that increases slower: a qualitatively similar unbinding process is observed (Fig.6.4).

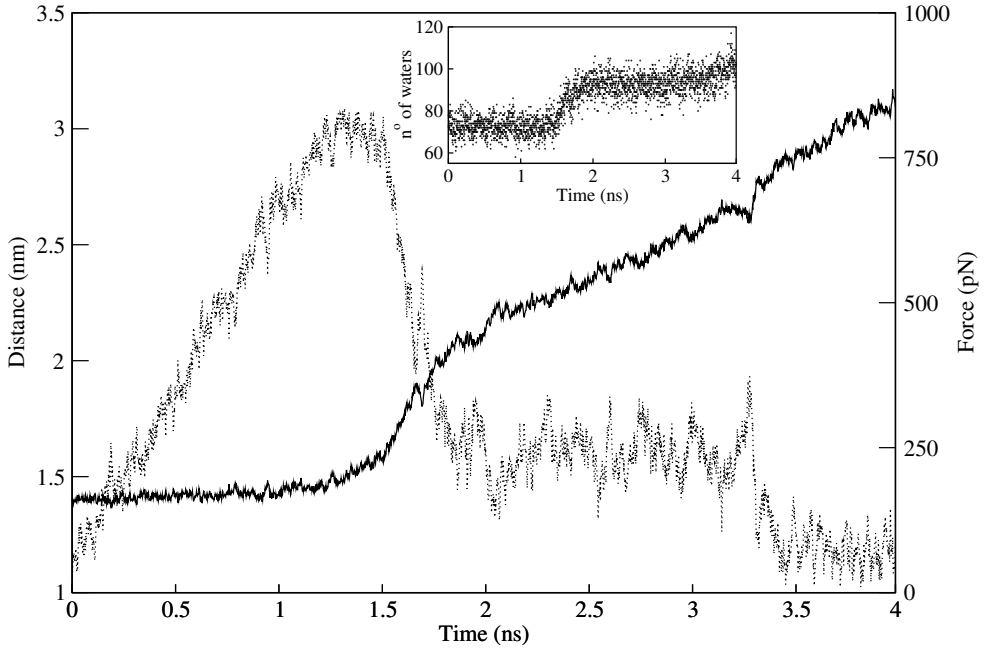

Figure 6.4: SMD of **c2**. The restraint point is moved at a velocity of 0.25 nm/ns, which is half the velocity of the steered MD in Fig.3. (a) Distance between the mass centers of trkA-d5 and of the peptide (solid line) and force on the peptide (dashed line) plotted as a function of the simulation time. The force increases with a rate of ∼0.61 pN/ps within the first 1.2 ns. All peptide/receptor interactions are broken after 1.5 ns of SMD except those formed by the peptide residues ARG9 and GLU11, which break down at about 1.75 ns and 3.3 ns of SMD respectively. The insert shows the number of water oxygens within 0.45 nm of non-hydrogen atoms of the peptide residues, as a function of the simulation time.

After a total of 3 ns of SMD, the peptide is unbound from the receptor and further 5.4 ns of MD are performed, without applying external force to the peptide (Fig.6.3c). The mean RMSD calculated for the receptor is 0.14 (0.02) nm and the conformation of the unbound trkA-d5 is very similar to that of the receptor bound to NGF [260];

the mean RMSD for the peptide is 0.30 (0.05) nm (Fig.6.3d).

By performing 25 ns of MD simulation of the peptide, we observe that the peptide is folding into itself progressively: the RMSD is 0.26 nm at 0 ns and 0.20 nm at 25 ns. ARG9 and GLU11 do not form an intra-peptide salt bridge neither here nor in the previous complexes; two intra-peptide H-bonds, between ILE6 N and HIS4 Nδ and between PHE7 N and HIS4 O are maintained during the dynamics. The side chains are oriented as in the bound peptide, with the exception of GLU11 side chain, that interacts with the backbone of the peptide C-term part.

6.3 Concluding remarks

Our simulations suggest that the $_{ACE}HPIFGRGEF_{NME}$ peptide may provide high affinity to the trkA-d5 receptor, as all the residues form interactions with the receptor except the GLY8 and GLY10 residues; however, the latter provides conformational flexibility which allows the peptide to form an additional interaction with the receptor.

SMD calculations suggest that the strengths of the contacts between the peptide and its target are similar, with the exception of the salt bridges formed by ARG9 and GLU11 with trkA-d5 (Fig.6.1c). These interactions are the most persistent in the SMD, possibly because of the large flexibility and length of the side chains involved, which can rearrange so as to maintain the electrostatic interactions despite the increase of the peptide/receptor distance, with respect to all the other residues at the interface.

The challenge is now to perform *in vitro* and *in vivo* experiments which may quantify the actual efficacy of this peptide as an agonist or competitive antagonist [261,175].

6.4 Reference

The work reported in the present chapter has been published in the following article: Marco Berrera, Antonino Cattaneo and Paolo Carloni. *"Molecular simulation of the binding of nerve growth factor peptide mimics to the receptor tyrosine kinase A"* Biophysical Journal (2006) 91:2063-2071.

Chapter 7

Conclusions

The calculations presented in this thesis have provided some examples of the use of molecular simulation as a tool for structural biology and ligand design, complementary to experimental techniques, such as X-ray crystallography and NMR.

First, we have used MD simulations to investigate the structural features of **the bacterial transcription activator protein CAP** in aqueous solution. Our calculations suggest that crystal packing contacts modify the conformation of CAP so that the DNA Binding Domains (DBD) are differently arranged. On the contrary, the homodimer in solution assumes a symmetric arrangement in which both DBDs are separated from the respective Cyclic Nucleotide Binding Domain (CNBD) by a cleft. We speculate that CAP in this *open* conformation is the ligand-activated form of the protein, which is important to mediate the first step in the interaction with the target DNA, and that the rearrangement to the *closed* conformation, which is observed in the DNA-bound X-ray structures, is favoured by the larger electrostatic complementarity with DNA of the protein in this state.

Subsequently, we have investigated the dynamic features of **the intracellular part of the HCN2 channel**. The motion of the cAMP-bound intracellular part of the HCN2 channel, which is responsible for the channel modulation upon binding of the ligand cAMP, is characterized by a $\backsim$10 ns quaternary structure oscillation hinged at the intersubunit contact surface. Elastic network analysis supports these conclusions. This large-scale oscillation is here proposed to play an important role for the protein function, being coupled to a motion of the C-linker which, in turn, modulates the

gating of the channel. The MD simulations provide also insights on the cytoplasmic domains in the ligand free form, for which no structural information is available. CNBD experiences a cascade of rearrangements of secondary structure elements, starting from the binding pocket, as similarly described for the CNBDs of other different proteins. Thus, MD simulations allow us to dissect aspects of the mechanism for cAMP allosteric modulation in the HCN2 channel.

The last part of this thesis deals with the structure-based design of **a NGF peptide mimic with high affinity for its target receptor trkA**. The simulations suggest that the $_{ACE}$*HPIFGRGEF*$_{NME}$ peptide may specifically bind with high affinity to trkA, as most residues form stabilizing interactions with the target. Steered MD calculations suggest that the strengths of the contacts between the peptide and trkA are similar, with the exception of two salt bridges formed by the arginine and the glutamate residues with the receptor. These interactions turned out to be the most persistent, possibly because of the large flexibility and length of the side chains involved, which can rearrange so as to maintain the electrostatic interactions despite the increase of the peptide/receptor distance. Experiments will be performed in the laboratory of Prof. Cattaneo to measure the actual efficacy of this peptide as a trkA binder.

In conclusion, computational techniques have been applied to the study of a variety of biological systems, providing insights into their structural, dynamic and energetic features. The theoretical analysis gives information about conformational changes, fluctuations and ligand binding affinities, complementary to the strctural information obtained by X-ray crystallography.

List of Figures

List of Tables

Bibliography

[1] Cheatham TE 3rd and Kollman PA. Molecular dynamics simulation of nucleic acids. *Annu Rev Phys Chem*, 51:435–471, 2000.

[2] Sansom MS, Shrivastava IH, Bright JN, Tate J, Capener CE, and Biggin PC. Potassium channels: structures, models, simulations. *Biochim Biophys Acta*, 1565(2):294–307, 2002.

[3] Hansson T, Oostenbrink C, and van Gunsteren W. Molecular dynamics simulations. *Curr Opin Struct Biol*, 12(2):190–196, 2002.

[4] Karplus M and McCammon JA. Molecular dynamics simulations of biomolecules. *Nat Struct Biol*, 9(9):646–652, 2002.

[5] Karplus M. Molecular dynamics simulations of biomolecules. *Acc Chem Res*, 35(6):321–323, 2002.

[6] Domene C, Bond PJ, and Sansom MS. Membrane protein simulations: ion channels and bacterial outer membrane proteins. *Adv Protein Chem*, 66:159–193, 2003.

[7] Bond PJ and Sansom MS. The simulation approach to bacterial outer membrane proteins. *Mol Membr Biol*, 21:151–161, 2004.

[8] S A Adcock and J A McCammon. Molecular dynamics: survey of methods for simulating the activity of proteins. *Chem Rev*, 106(5):1589–1615, 2006.

[9] C Micheletti, P Carloni, and A Maritan. Accurate and efficient description of protein vibrational dynamics: comparing molecular dynamics and gaussian models. *Proteins*, 55:635–645, 2004.

[10] Wong CF and McCammon JA. Protein flexibility and computer-aided drug design. *Annu Rev Pharmacol Toxicol*, 43:31–45, 2003.

[11] Gervasio FL, Laio A, and Parrinello M. Flexible docking in solution using metadynamics. *J Am Chem Soc*, 127(8):2600–2607, 2005.

[12] Sansom MS. Models and simulations of ion channels and related membrane proteins. *Curr Opin Struct Biol*, 8:237–244, 1998.

[13] CE Capener, HJ Kim, Y Arinaminpathy, and MS Sansom. Ion channels: structural bioinformatics and modelling. *Hum Mol Genet*, 11:2425–2433, 2002.

[14] A Giorgetti and P Carloni. Molecular modeling of ion channels: structural predictions. *Curr Opin Chem Biol*, 7:150–156, 2003.

[15] Beckstein O, Biggin PC, Bond P, Bright JN, Domene C, Grottesi A, Holyoake J, and Sansom MS. Ion channel gating: insights via molecular simulations. *FEBS Lett*, 555(1):85–90, 2003.

[16] Oldziej S, Czaplewski C, Liwo A, Chinchio M, Nanias M, Vila JA, Khalili M, Arnautova YA, Jagielska A, Makowski M, Schafroth HD, Kazmierkiewicz R, Ripoll DR, Pillardy J, Saunders JA, Kang YK, Gibson KD, and Scheraga HA. Physics-based protein-structure prediction using a hierarchical protocol based on the unres force field: assessment in two blind tests. *Proc Natl Acad Sci U S A*, 102(21):7547–7552, 2005.

[17] Bond PJ and Sansom MS. Insertion and assembly of membrane proteins via simulation. *J Am Chem Soc*, 128:2697–2704, 2006.

[18] Johnston JM, Cook GA, Tomich JM, and Sansom MS. Conformation and environment of channel-forming peptides: a simulation study. *Biophys J*, 90:1855–1864, 2006.

[19] Arkhipov A, Freddolino PL, Imada K, Namba K, and Schulten K. Coarse-grained molecular dynamics simulations of a rotating bacterial flagellum. *Biophys J*, 2006.

[20] Pellarin R and Caflisch A. Interpreting the aggregation kinetics of amyloid peptides. *J Mol Biol*, 360:882–892, 2006.

[21] Balaeff A, Mahadevan L, and Schulten K. Modeling DNA loops using the theory of elasticity. *Phys Rev E*, 73:031919, 2006.

[22] H M Berman, J Westbrook, Z Feng, G Gilliland, T N Bhat, H Weissig, I N Shindyalov, and P E Bourne. The Protein Data Bank. *Nucleic Acids Research*, 28:235–242, 2000.

[23] J M Passner, S C Schultz, and T A Steitz. Modeling the cAMP-induced allosteric transition using the crystal structure of CAP-cAMP at 2.1 A resolution. *J Mol Biol*, 304:847–859, 2000.

[24] Piana S, Carloni P, and Parrinello M. Role of conformational fluctuations in the enzymatic reaction of hiv-1 protease. *J Mol Biol*, 319(2):567–583, 2002.

[25] Pang A, Arinaminpathy Y, Sansom MS, and Biggin PC. Comparative molecular dynamics–similar folds and similar motions? *Proteins*, 61(4):809–822, 2005.

[26] Carnevale V and Carloni P Raugei Sand Micheletti C and. Convergent dynamics in the protease enzymatic superfamily. *J Am Chem Soc*, 128(30):9766–9772, 2006.

[27] WN Zagotta, NB Olivier, KD Black, EC Young, R Olson, and E Gouaux. Structural basis for modulation and agonist specificity of HCN pacemaker channels. *Nature*, 425:200–205, 2003.

[28] C Wiesmann, MH Ultsch, SH Bass, and AM de Vos. Crystal structure of nerve growth factor in complex with the ligand-binding domain of the TrkA receptor. *Nature*, 401:184–188, 1999.

[29] J L Botsford and J G Harman. Cyclic amp in prokaryotes. *Microbiol Rev*, 56(1):100–122, 1992.

[30] Kolb A, Busby S, Buc H, Garges S, and Adhya S. Transcriptional regulation by cAMP and its receptor protein. *Annu Rev Biochem*, 62:749–795, 1993.

[31] S Adhya, S Ryu, and S Garges. Role of allosteric changes in cyclic AMP receptor protein function. *Subcell Biochem*, 24:303–321, 1995.

[32] J G Harman. Allosteric regulation of the cAMP receptor protein. *Biochim Biophys Acta*, 1547:1–17, 2001.

[33] Lawson CL, Swigon D, Murakami KS, Darst SA, Berman HM, and Ebright RH. Catabolite activator protein: DNA binding and transcription activation. *Curr Opin Struct Biol*, 14:10–20, 2004.

[34] S Garges and S Adhya. Sites of allosteric shift in the structure of the cyclic AMP receptor protein. *Cell*, 41:745–751, 1985.

[35] Scott SP and Jarjous S. Proposed structural mechanism of Escherichia coli cAMP receptor protein cAMP-dependent proteolytic cleavage protection and selective and nonselective DNA binding. *Biochemistry*, 44:8730–8748, 2005.

[36] Krakow JS and Pastan I. Cyclic adenosine monophosphate receptor: loss of cAMP-dependent DNA binding activity after proteolysis in the presence of cyclic adenosine monophosphate. *Proc Natl Acad Sci U S A*, 70:2529–2533, 1973.

[37] Busby S and Ebright RH. Transcription activation by catabolite activator protein (CAP). *J Mol Biol*, 293:199–213, 1999.

[38] Heyduk T and Lee JC. Escherichia coli cAMP receptor protein: evidence for three protein conformational states with different promoter binding affinities. *Biochemistry*, 28:6914–6924, 1989.

[39] Heyduk T and Lee J C. Application of fluorescence energy transfer and polarization to monitor escherichia coli cAMP receptor protein and lac promoter interaction. *Proc Natl Acad Sci U S A*, 87:1744–1748, 1990.

[40] Chattopadhyay R and Parrack P. Cyclic AMP-dependent functional forms of cyclic AMP receptor protein from Vibrio cholerae. *Arch Biochem Biophys*, 2006.

[41] J M Passner and T A Steitz. The structure of a CAP-DNA complex having two cAMP molecules bound to each monomer. *Proc Natl Acad Sci U S A*, 94:2843–2847, 1997.

[42] Lin SH and Lee JC. Communications between the high-affinity cyclic nucleotide binding sites in E. coli cyclic AMP receptor protein: effect of single site mutations. *Biochemistry*, 41:11857–11867, 2002.

[43] S C Schultz, G C Shields, and T A Steitz. Crystal structure of a CAP-DNA complex: the DNA is bent by 90 degrees. *Science*, 253:1001–1007, 1991.

[44] Chen S, Gunasekera A, Zhang X, Kunkel TA, Ebright RH, and Berman HM. Indirect readout of DNA sequence at the primary-kink site in the CAP-DNA complex: alteration of DNA binding specificity through alteration of DNA kinking. *J Mol Biol*, 314:75–82, 2001.

[45] Lanzilotta WN, Schuller DJ, Thorsteinsson MV, Kerby RL, Roberts GP, and Poulos TL. Structure of the CO sensing transcription activator CooA. *Nat Struct Biol*, 7:876–880, 2000.

[46] H M Berman, L F Ten Eyck, D S Goodsell, N M Haste, A Kornev, and S S Taylor. The cAMP binding domain: an ancient signaling module. *Proc Natl Acad Sci U S A*, 102:45–50, 2005.

[47] S Pantano, M Zaccolo, and P Carloni. Molecular basis of the allosteric mechanism of cAMP in the regulatory PKA subunit. *FEBS Letters*, 579:2679–2685, 2005.

[48] Berrera M, Pantano S, and Carloni P. cAMP modulation of the cytoplasmic domain in the HCN2 channel investigated by molecular simulation. *Biophys J*, 2006.

[49] Aiba H, Nakamura T, Mitani H, and Mori H. Mutations that alter the allosteric nature of cAMP receptor protein of Escherichia coli. *EMBO J*, 4:3329–3332, 1985.

[50] Kim J, Adhya S, and Garges S. Allosteric changes in the cAMP receptor protein of Escherichia coli: hinge reorientation. *Proc Natl Acad Sci U S A*, 89:9700–9704, 1992.

[51] S Ryu, J Kim, S Adhya, and S Garges. Pivotal role of amino acid at position 138 in the allosteric hinge reorientation of cAMP receptor protein. *Proc Natl Acad Sci U S A*, 90:75–79, 1993.

[52] N Baichoo and T Heyduk. Mapping conformational changes in a protein: application of a protein footprinting technique to cAMP-induced conformational changes in cAMP receptor protein. *Biochemistry*, 36:10830–6, 1997.

[53] Krueger S, Gorshkova I, Brown J, Hoskins J, McKenney KH, and Schwarz FP. Determination of the conformations of cAMP receptor protein and its T127L, S128A mutant with and without cAMP from small angle neutron scattering measurements. *J Biol Chem*, 273:20001–20006, 1998.

[54] Malecki J, Polit A, and Wasylewski Z. Kinetic studies of cAMP-induced allosteric changes in cyclic AMP receptor protein from Escherichia coli. *J Biol Chem*, 275:8480–8486, 2000.

[55] Won HS, Yamazaki T, Lee TW, Yoon MK, Park SH, Kyogoku Y, and Lee BJ. Structural understanding of the allosteric conformational change of cyclic AMP receptor protein by cyclic AMP binding. *Biochemistry*, 39:13953–13962, 2000.

[56] M. K. Chan. CooA, CAP and allostery. *Nat Struct Biol*, 7:822–824, 2000.

[57] Dong A, Malecki JM, Lee L, Carpenter JF, and Lee JC. Ligand-induced conformational and structural dynamics changes in Escherichia coli cyclic AMP receptor protein. *Biochemistry*, 41:6660–6667, 2002.

[58] H Youn, R L Kerby, M Conrad, and G P Roberts. Study of Highly Constitutively Active Mutants Suggests How cAMP Activates cAMP Receptor Protein. *J Biol Chem*, 281(2):1119–1127, 2006.

[59] O G Berg and P H von Hippel. Selection of DNA binding sites by regulatory proteins. II. The binding specificity of cyclic AMP receptor protein to recognition sites. *J Mol Biol*, 200(4):709–723, 1988.

[60] Kahn JD and Crothers DM. Protein-induced bending and DNA cyclization. *Proc Natl Acad Sci U S A*, 89:6343–6347, 1992.

[61] Heyduk T and Lee JC. Solution studies on the structure of bent DNA in the cAMP receptor protein-lac DNA complex. *Biochemistry*, 31:5165–5171, 1992.

[62] Kahn JD and Crothers DM. Measurement of the DNA bend angle induced by the catabolite activator protein using Monte Carlo simulation of cyclization kinetics. *J Mol Biol*, 276:287–309, 1998.

[63] Dixit S B, Andrews D Q, and Beveridge D L. Induced fit and the entropy of structural adaptation in the complexation of CAP and lambda-repressor with cognate DNA sequences. *Biophys J*, 88:3147–3157, 2005.

[64] Dixit S B and Beveridge D L. Axis curvature and ligand induced bending in the CAP-DNA oligomers. *Biophys J*, 88:L04–L06, 2005.

[65] W K Olson, A A Gorin, X J Lu, L M Hock, and V B Zhurkin. Dna sequence-dependent deformability deduced from protein-dna complexes. *Proc Natl Acad U S A*, 95:11163–11168, 1998.

[66] Y Zhou, X Zhang, and R H Ebright. Identification of the activating region of catabolite gene activator protein (CAP): isolation and characterization of mutants of CAP specifically defective in transcription activation. *Proc Natl Acad Sci U S A*, 90(13):6081–6085, 1993.

[67] R Jin, K A Sharif, and J S Krakow. Evidence for contact between the cyclic AMP receptor protein and the delta 70 subunit of Escherichia coli RNA polymerase. *J Biol Chem*, 270(33):19213–19216, 1995.

[68] W Niu, Y Kim, G Tau, T Heyduk, and R H Ebright. Transcription activation at class II CAP-dependent promoters: two interactions between CAP and RNA polymerase. *Cell*, 87(6):1123–1134, 1996.

[69] L Sogaard-Andersen, A S Mironov, H Pedersen, W Sukhodelets, and P Valentin-Hansen. Single amino acid substitutions in the cAMP receptor protein specifically abolish regulation by the CytR repressor in Escherichia coli. *Proc Natl Acad Sci U S A*, 88(11):4921–4925, 1991.

[70] N Baichoo and T Heyduk. DNA-induced conformational changes in cyclic AMP receptor protein: detection and mapping by a protein footprinting technique using multiple chemical proteases. *J MolBiol*, 290(1):37–48, 1999.

[71] J A Lefstin and K R Yamamoto. Allosteric effects of DNA on transcriptional regulators. *Nature*, 392(6679):885–888, 1998.

[72] B Hille. *Ion channels of excitable membranes.* Sunderland, Mass. Sinauer Associates, 2001.

[73] W A Catterall. From ionic currents to molecular mechanisms: the structure and function of voltage-gated sodium channels. *Neuron*, 26:13–25, 2000.

[74] Z Sands, A Grottesi, and M S Sansom. Voltage-gated ion channels. *Curr Biol*, 15(2):44–47, 2005.

[75] F Bezanilla. Voltage-gated ion channels. *IEEE Trans Nanobioscience*, 4(1):34–48, 2005.

[76] G Chang, R H Spencer, A T Lee, M T Barclay, and D C Rees. Structure of the MscL homolog from Mycobacterium tuberculosis: a gated mechanosensitive ion channel. *Scince*, 282:2220–2226, 1998.

[77] J Bradley, J Reisert, and S Frings. Regulation of cyclic nucleotide-gated channels. *Curr Opin Neurobiol*, 15(3):343–349, 2005.

[78] K Matulef and W N Zagotta. Cyclic nucleotide-gated ion channels. *Annu Rev Cell Dev Biol*, 19:23–44, 2003.

[79] L G Cuello, J G Romero, D M Cortes, and E Perozo. pH-dependent gating in the Streptomyces lividans K+ channel. *Biochemistry*, 37:3229–3236, 1998.

[80] B Corry and S H Chung. Mechanisms of valence selectivity in biological ion channels. *Cell Mol Life Sci*, 63(3):301–315, 2006.

[81] T J Jentsch, W Gunther, M Pusch, and B Schwappach. Properties of voltage-gated chloride channels of the ClC gene family. *J. Physiol*, 482:19S–25S, 1995.

[82] A HStam, J Haan, R R Frants, M D Ferrari, and A M van den Maagdenberg. Migraine: new treatment options from molecular biology. *Expert Rev Neurother*, 5(5):653–661, 2005.

[83] A L Jr George. Inherited disorders of voltage-gated sodium channels. *J Clin Invest*, 115(8):1990–1999, 2005.

[84] D Corrado, C Basso, and G Thiene. Is it time to include ion channel diseases among cardiomyopathies? *J Electrocardiol*, 38(4 Suppl):81–87, 2005.

[85] J C Mulley, I E Scheffer, L A Harkin, S F Berkovic, and L M Dibbens LM. Susceptibility genes for complex epilepsy. *Hum Mol Genet*, 14(Spec No 2):243–249, 2005.

[86] M Shah, F G Akar, and G F Tomaselli GF. Molecular basis of arrhythmias. *Circulation*, 112(16):2517–2529, 2005.

[87] R Roberts and R Brugada. Genetics and arrhythmias. *Annu Rev Med*, 54:257–267, 2003.

[88] S F Berkovic and I E Scheffer. Genetics of the epilepsies. *Epilepsia*, 42(Suppl 5):16–23, 2001.

[89] P Mistrik, R Mader, S Michalakis, M Weidinger, A Pfeifer, and M Biel. The murine HCN3 gene encodes a hyperpolarization-activated cation channel with slow kinetics and unique response to cyclic nucleotides. *J Biol Chem*, 280:27056–27061, 2005.

[90] X Yu, KL Duan, CF Shang, HG Yu, and Z Zhou. Calcium influx through hyperpolarization-activated cation channels (I(h) channels) contributes to activity-evoked neuronal secretion. *Proc Natl Acad Sci U S A*, 101:1051–1056, 2004.

[91] T Rosenbaum and S E Gordon. Quickening the pace: looking into the heart of HCN channels. *Neuron*, 42:193–196, 2004.

[92] J Stieber, S Herrmann, S Feil, J Loster, R Feil, M Biel, F Hofmann, and A Ludwig. The hyperpolarization-activated channel HCN4 is required for the generation of pacemaker action potentials in the embryonic heart. *Proc Natl Acad Sci U S A*, 100:15235–15240, 2003.

[93] R B Robinson and S A Siegelbaum. Hyperpolarization-activated cation currents: from molecules to physiological function. *Annu Rev Physiol*, 65:453–480, 2003.

[94] M Biel, A Schneider, and C Wahl. Cardiac HCN channels: structure, function, and modulation. *Trends Cardiovasc Med*, 12:206–212, 2002.

[95] J Chen, DR Piper, and MC Sanguinetti. Voltage sensing and activation gating of HCN pacemaker channels. *Trends in Cardiovascular Medicine*, 12:42–45, 2002.

[96] EA Accili, C Proenza, M Baruscotti, and D DiFrancesco. From funny current to HCN channels: 20 years of excitation. *News Physiol Sci*, 17:32–37, 2002.

[97] LY Jan and YN Jan. A superfamily of ion channels. *Nature*, 345:672, 1990.

[98] D DiFrancesco and P Tortora. Direct activation of cardiac pacemaker channels by intracellular cyclic AMP. *Nature*, 351:145–147, 1991.

[99] A Ludwig, X Zong, M Jeglitsch, F Hofmann, and M Biel. A family of hyperpolarization-activated mammalian cation channels. *Nature*, 393:587–591, 1998.

[100] B Santoro and G R Tibbs. The HCN gene family: molecular basis of the hyperpolarization-activated pacemaker channels. *Ann N Y Acad Sci*, 868:741–764, 1999.

[101] R Seifert, A Scholten, R Gauss, A Mincheva, P Lichter, and U B Kaupp. Molecular characterization of a slowly gating human hyperpolarization-activated channel predominantly expressed in thalamus, heart, and testis. *Proc Natl Acad Sci U S A*, 96:9391–9396, 1999.

[102] A Ludwig, X Zong, F Hofmann, and M Biel. Structure and function of cardiac pacemaker channels. *Cell Physiol Biochem*, 9:179–186, 1999.

[103] BJ Wainger, M DeGennaro, B Santoro, SA Siegelbaum, and GR Tibbs. Molecular mechanism of cAMP modulation of HCN pacemaker channels. *Nature*, 411:805–810, 2001.

[104] J Wang, S Chen, and SA Siegelbaum. Regulation of hyperpolarization-activated HCN channel gating and cAMP modulation due to interactions of COOH terminus and core transmembrane regions. *J Gen Physiol*, 118:237–250, 2001.

[105] D DiFrancesco. Pacemaker mechanisms in cardiac tissues. *Annu. Rev. Physiol.*, 55:455–472, 1993.

[106] H Pape. Queer current and pacemaker: the hyperpolarization-activated cation currents in neurons. *Annu. Rev. Physiol.*, 58:299–327, 1996.

[107] H Brown and W Ho. *The hyperpolarization-activated inward channel and cardiac pacemaker activity.* Kluwer, Dordrecht, The Netherlands, molecular physiology and pharmacology of cardiac ion channels and transporters edition, 1996. 17-30.

[108] J Halliwell and P Adams. Voltage-clamp analysis of muscarinic excitation in hippocampal neurons. *Brain. Res.*, 250:71–92, 1982.

[109] A Noma and H Irisawa. Membrane currents in the rabbit sinoatrial node cell as studied by the double microelectrode method. *Pflugers Arch.*, 364:45–52, 1976.

[110] H F Brown, D DiFrancesco, and S J Noble. How does adrenaline accelerate the heart? *Nature*, 280:235–236, 1979.

[111] D Clapham. Not so funny anymore: pacing channels are cloned. *Neuron*, 21:5, 1998.

[112] L Wollmuth and B Hille. Ionic selectivity of ih channels of rod photoreceptors in tiger salamanders. *J. Gen. Physiol .*, 100:749–765, 1992.

[113] W Ho, H Brown, and D Noble. High selectivity of the If channels to Na+ and K+ in rabbit isolated sinoatrial node cells. *Pflugers Arch.*, 426:68–74, 1994.

[114] G Fain, F Quandt, B Bastian, and H M Gerschenfeld. Contribution of a cesium-sensitive conductance increase to the rod photoresponse. *Nature*, 272:466–469, 1978.

[115] S Chen, J Wang, and S A Siegelbaum. Properties of hyperpolarization-activated pacemaker current defined by coassembly of HCN1 and HCN2 subunits and basal modulation by cyclic nucleotide. *J Gen Physiol*, 117(5):491–504, 2001.

[116] U B Kaupp and R Seifert. Molecular diversity of pacemaker ion channels. *Annu Rev Physiol*, 63:235–257, 2001.

[117] R Gauss, R Seifert, and U B Kaupp. Molecular identification of a hyperpolarization-activated channel in sea urchin sperm. *Nature*, 393(6685):583–587, 1998.

[118] J Krieger, J Strobel, A Vogl, W Hanke, and H Breer. Identification of a cyclic nucleotide- and voltage-activated ion channel from insect antennae. *Insect Biochem Mol Biol*, 29(3):255–267, 1999.

[119] T Marx, G Gisselmann, K F Strtkuhl, B T Hovemann, and H Hatt. Molecular cloning of a putative voltage- and cyclic nucleotide-gated ion channel present in the antennae and eyes of Drosophila melanogaster. *Invertebrate Neuroscience*, 4(1):55–63, 1999.

[120] G Gisselmann, M Warnstedt, B Gamerschlag, A Bormann, T Marx, E M Neuhaus, K Stoertkuhl, C H Wetzel, and H Hatt. Characterization of recombinant and native Ih-channels from Apis mellifera. *Insect Biochem Mol Biol*, 33(11):1123–1134, 2003.

[121] JP Jr Johnson and WN Zagotta. The carboxyl-terminal region of cyclic nucleotide-modulated channels is a gating ring, not a permeation path. *Proc Natl Acad Sci U S A*, 102:2742–2747, 2005.

[122] GM Clayton, WR Silverman, L Heginbotham, and JH Morais-Cabral. Structural basis of ligand activation in a cyclic nucleotide regulated potassium channel. *Cell*, 119:615–627, 2004.

[123] SS Taylor, J Yang, J Wu, NM Haste, E Radzio-Andzelm, and G Anand. PKA: a portrait of protein kinase dynamics. *Biochim Biophys Acta*, 1697:259–269, 2004.

[124] J Wu, S Brown, NH Xuong, and SS Taylor. RI-alpha subunit of PKA: a cAMP-free structure reveals a hydrophobic capping mechanism for docking cAMP into site B. *Structure (Camb)*, 12:1057–1065, 2004.

[125] H Rehmann, B Prakash, E Wolf, A Rueppel, J De Rooij, J L Bos, and A Wittinghofer. Structure and regulation of the cAMP-binding domains of Epac2. *Nat Struct Biol*, 10:26–32, 2003.

[126] T C Diller, N H Madhusudan Xuong, and S S Taylor. Molecular basis for regulatory subunit diversity in cAMP-dependent protein kinase: crystal structure of the type II beta regulatory subunit. *Structure (Camb)*, 9:73–82, 2001.

[127] Y Su, WR Dostmann, FW Herberg, K Durick, NH Xuong, L Ten Eyck, SS Taylor, and KI Varughese. Regulatory subunit of protein kinase A: structure of deletion mutant with cAMP binding domains. *Science*, 269:807–813, 1995.

[128] G R Lewin and Y A Barde. Physiology of the neurotrophins. *Annu Rev Neurosci*, 19:289–317, 1996.

[129] M Bibel and Y A Barde YA. Neurotrophines: key regulators of cell fate and cell shape in the vertebrate nervous system. *Genes and Develpment*, 14:2919–2937, 2000.

[130] R. Kalb. The protean actions of neurotrophins and their receptors on the life and death of neurons. *Trends Neurosci*, 28:5–11, 2005.

[131] Dechant G and Neumann H. Neurotrophins. *Adv Exp Med Biol*, 513:303–334, 2002.

[132] J M Frade and Y A Barde. Nerve growth factor: two receptors, multiple functions. *Bioessays*, 20:137–145, 1998.

[133] Chao M, Casaccia-Bonnefil P, Carter B, Chittka A, Kong H, and Yoon SO. Neurotrophin receptors: mediators of life and death. *Brain Res Brain Res Rev*, 26:295–301, 1998.

[134] Patapoutian A and Reichardt LF. Trk receptors: mediators of neurotrophin action. *Curr. opinion Neurobiol.*, 11:272–280, 2001.

[135] E J Huang and L F Reichardt. Trk receptors: roles in neuronal signal transduction. *Annu Rev Biochem*, 72:609–642, 2003.

[136] D R Kaplan, B L Hempstead, D Martin-Zanca, M V Chao, and L F Parada. The trk proto-oncogene product: a signal transducing receptor for nerve growth factor. *Science*, 252:554–558, 1991.

[137] R Klein, SQ Jing, V Nanduri, E O'Rourke, and M Barbacid. The trk proto-oncogene encodes a receptor for nerve growth factor. *Cell*, 65:189–197, 1991.

[138] M Barbacid. The trk family of neurotrophin receptors. *J Neurobiol*, 11:1386–1403, 1994.

[139] R Levi-Montalcini. The nerve growth factor: its mode of action on sensory and sympathetic nerve cells. *Harvey Lect*, 60:217–259, 1966.

[140] R A Bradshaw, T L Blundell, R Lapatto, N Q McDonald, and J Murray-Rust. Nerve growth factor revisited. *Trends Biochem Sci.*, 18:48–52, 1993.

[141] C Wiesmann and A M De Vos. Nerve growth factor: structure and function. *Cell. Mol. Life Sci.*, 58:748–759, 2001.

[142] A. Brancucci, N. Kuczewski, S. Covaceuszach, A. Cattaneo, and L. Domenici. Nerve growth factor favours long-term depression over long-term potentiation in layer II-III neurones of rat visual cortex. *J Physiol*, 559:497–506, 2004.

[143] R Levi-Montalcini and B Booker. Destruction of the sympathetic ganglia in mammals by an antiserum to a nerve-growth protein. *PNAS Proceedings of the National Academy of Sciences USA*, 46:384–391, 1960.

[144] P U Angeletti, R Levi-Montalcini, and F Caramia. Ultrastructural changes in sympathetic neurons of newborn and adult mice treated with nerve growth factor. *J Ultrastruct Res*, 36(1):24–36, 1971.

[145] R Levi-Montalcini, R Dal Toso, F della Valle, S D Skaper, and A Leon. Update of the NGF saga. *J Neurol Sci*, 130(2):119–127, 1995.

[146] P Calissano, A Cattaneo, S Biocca, L Aloe, D Mercanti, and R Levi-Montalcini. The nerve growth factor. established findings and controversial aspects. *Exp Cell Res*, 154(1):1–9, 1984.

[147] A J Reynolds, S E Bartlett, and I A Hendry. Molecular mechanisms regulating the retrograde axonal transport of neurotrophins. *Brain Res Brain Res Rev*, 33(2-3):169–178, 2000.

[148] K E Neet and R B Campenot. Receptor binding, internalization, and retrograde transport of neurotrophic factors. *Cell Mol Life Sci*, 58:1021–1035, 2001.

[149] D E Timm and K E Neet. Equilibrium denaturation studies of mouse beta-nerve growth factor. *Protein Sci*, 1:236–244, 1992.

[150] N Q McDonald, R Lapatto, J Murray-Rust, J Gunning, A Wlodawer, and T L Blundell. New protein fold revealed by a 2.3-A resolution crystal structure of nerve growth factor. *Nature*, 354(6352):411–414, 1991.

[151] K K Teng and B L Hempstead. Neurotrophins and their receptors: signaling trios in complex biological systems. *Cell Mol Life Sci*, 61:35–48, 2004.

[152] M V Chao. Neurotrophins and their receptors: a convergence point for many signalling pathways. *Nat Rev Neurosci*, 4:299–309, 2003.

[153] M V Chao, M A Bothwell, A H Ross, H Koprowski, A A Lanahan, C R Buck, and A Sehgal. Gene transfer and molecular cloning of the human NGF receptor. *Science*, 232:518–521, 1986.

[154] B L Hempstead, D Martin-Zanca, D R Kaplan, L F Parada, and M V Chao. High-affinity NGF binding requires coexpression of the trk proto-oncogene and the low-affinity NGF receptor. *Nature*, 350:678–683, 1991.

[155] R Lee, P Kermani, K K Teng, and B L Hempstead. Regulation of cell survival by secreted proneurotrophins. *Science*, 294:1945–1948, 2001.

[156] B L Hempstead. The many faces of p75NTR. *Current Opinion in Neurobiology*, 12:260–267, 2002.

[157] Urfer R, Tsoulfas P, O'Connell L, Hongo JA, Zhao W, and Presta LG. High resolution mapping of the binding site of TrkA for nerve growth factor and TrkC for neurotrophin-3 on the second immunoglobulin-like domain of the Trk receptors. *J Biol Chem*, 273:5829–5840, 1998.

[158] P Kahle, L E Burton, C H Schmelzer, and C Hertel. The amino terminus of nerve growth factor is involved in the interaction with the receptor tyrosine kinase p140trkA. *J Biol Chem*, 267:22707–22710, 1992.

[159] C F Ibanez, L L Ilag, J Murray-Rust, and H Persson. An extended surface of binding to trk tyrosine kinase receptors in NGF and BDNF allows the engineering of a multifunctional pan-neurotrophin. *EMBO J*, 12:2281–2293, 1993.

[160] Shih A, Laramee GR, Schmelzer CH, Burton LE, and Winslow JW. Mutagenesis identifies amino-terminal residues of nerve growth factor necessary for trk receptor binding and biological activity. *J Biol Chem*, 269:27679–27686, 1994.

[161] Treanor JJ, Schmelzer C, Knusel B, Winslow JW, Shelton DL, Hefti F, Nikolics K, and Burton LE. Heterodimeric neurotrophins induce phosphorylation of trk receptors and promote neuronal differentiation in PC12 cells. *J Biol Chem*, 270:23104–23110, 1995.

[162] N Q McDonald and M V Chao. Structural determinants of neurotrophin action. *J Biol Chem*, 270:19669–19672, 1995.

[163] C McInnes and B D Sykes. Growth factor receptors: strcture, mechanism and drug discovery. *Biopolymers*, 43:339–366, 1997.

[164] M J Banfield, R L Naylor, A G Robertson, S J Allen, D Dawbarn, and R L Brady. Specificity in Trk receptor:neurotrophin interactions: the crystal structure of TrkB-d5 in complex with neurotrophin-4/5. *Structure*, 9:1191–1199, 2001.

[165] G Settanni, A Cattaneo, and P Carloni. Molecular dynamics simulations of the NGF-TrkA domain 5 complex and comparison with biological data. *Biophys J*, 84:2282–2292, 2003.

[166] D R Holland, L S Cousens, W Meng, and B W Matthews. Nerve growth factor in different crystal forms displays structural flexibility and reveals zinc binding sites. *J Mol Biol*, 239(3):385–400, 1994.

[167] F Hefti. Pharmacology of neurotrophic factors. *Annu. Rev. Pharmacol. Toxicol.*, 37:239–267, 1997.

[168] T Hagg, M Manthorpe, H L Vahlsing, and S Varon. Delayed treatment with nerve growth factor reverses the apparent loss of cholinergic neurons after acute brain damage. *Exp Neurol*, 101:303–312, 1988.

[169] Apfel SC, Kessler JA, Adornato BT, Litchy WJ, Sanders C, and Rask CA. Recombinant human nerve growth factor in the treatment of diabetic polyneuropathy. NGF study group. *Neurology*, 51:695–702, 1998.

[170] M E Jonhagen. Nerve growth factor treatment in dementia. *Alzheimer Dis Assoc Disord*, 14 Suppl 1:31–38, 2000.

[171] M. H. Tuszynski, L. Thal, M. Pay, D. P. Salmon, H. S. U, R. Bakay, P. Patel, A. Blesch, H. L. Vahlsing, G. Ho, G. Tong, S. G. Potkin, J. Fallon, L. Hansen, E. J. Mufson, J. H. Kordower, C. Gall, and J. Conner. A phase 1 clinical trial of nerve growth factor gene therapy for Alzheimer disease. *Nature Medicine*, 11:551–555, 2005.

[172] S. Capsoni, G. Ugolini, A. Comparini, F. Ruberti, N. Berardi, and A. Cattaneo. Alzheimer-like neurodegeneration in aged antinerve growth factor transgenic mice. *Proc Natl Acad Sci U S A*, 97:6826–6831, 2000.

[173] S. Capsoni, S. Giannotta, and A. Cattaneo. Nerve growth factor and galantamine ameliorate early signs of neurodegeneration in anti-nerve growth factor mice. *Proc Natl Acad Sci U S A*, 99:12432–12437, 2002.

[174] R. De Rosa, A. A. Garcia, C. Braschi, S. Capsoni, L. Maffei, N. Berardi, and A. Cattaneo. Intranasal administration of nerve growth factor (NGF) rescues recognition memory deficits in AD11 anti-NGF transgenic mice. *Proc Natl Acad Sci U S A*, 102:3811–3816, 2005.

[175] K. G. Halvorson, K. Kubota, M. A. Sevcik, T. H. Lindsay, J. E. Sotillo, J. R. Ghilardi, T. J. Rosol, L. Boustany, D. L. Shelton, and P. W. Mantyh. A blocking antibody to nerve growth factor attenuates skeletal pain induced by prostate tumor cells growing in bone. *Cancer Res*, 65:9426–9435, 2005.

[176] Poduslo JF and Curran GL. Permeability at the blood-brain and blood-nerve barriers of the neurotrophic factors: NGF, CNTF, NT-3, BDNF. *Brain Res Mol Brain Res*, 36:280–286, 1996.

[177] F. F. Hefti, A. Rosenthal, P. A. Walicke, S. Wyatt, G. Vergara, D. L. Shelton, and A. M. Davies. Novel class of pain drugs based on antagonism of NGF. *Trends Pharmacol Sci*, 27:85–91, 2005.

[178] Saragovi HU, Greene MI, Chrusciel RA, and Kahn M. Loops and secondary structure mimetics: development and applications in basic science and rational drug design. *Biotechnology (N Y)*, 10:773–778, 1992.

[179] H U Saragovi and K Gehring. Development of pharmacological agents for targeting neurotrophins and their receptors. *Trends Pharmacol Sci*, 21:93–98, 2000.

[180] S J Pollack and S J Harper. Small molecule trk receptor agonists and other neurotrophic factor mimetics. *Curr Drug Target CNS Neurol Disord*, 1:59–80, 2002.

[181] S M Massa, Y Xie, and F M Longo. Alzheimer's therapeutics: neurotrophin domain small molecule mimetics. *J Mol Neurosci*, 20:323–326, 2003.

[182] L LeSauteur, L Wei, B F Gibbs, and H U Saragovi. Small peptide mimics of nerve growth factor bind TrkA receptors and affect biological responses. *J Biol Chem*, 270:6564–6569, 1995.

[183] L LeSauteur, N K Cheung, R Lisbona, and H U Saragovi. Small molecule nerve growth factor analogs image receptors in vivo. *Nat Biotechnol*, 14:1120–1122, 1996.

[184] Xie Y, Tisi MA, Yeo TT, and Longo FM. Nerve growth factor (NGF) loop 4 dimeric mimetics activate ERK and AKT and promote NGF-like neurotrophic effects. *J Biol Chem*, 275:29868–29874, 2000.

[185] N Beglova, S Maliartchouk, I Ekiel, M C Zaccaro, H U Saragovi, and K Gehring. Design and solution structure of functional peptide mimetics of nerve growth factor. *J Med Chem*, 43:3530–3540, 2000.

[186] S Maliartchouk, Y Feng, L Ivanisevic, T Debeir, A C Cuello, K Burgess, and H U Saragovi. A designed peptidomimetic agonistic ligand of TrkA nerve growth factor receptors. *Mol Pharmacol*, 57:385–391, 2000.

[187] S Maliartchouk, T Debeir, N Beglova, A C Cuello, K Gehring, and H U Saragovi. Genuine monovalent ligands of TrkA nerve growth factor receptors reveal a novel pharmacological mechanism of action. *J Biol Chem*, 275:9946–9956, 2000.

[188] M. C. Zaccaro, H. B. Lee, M. Pattarawarapan, Z. Xia, A. Caron, P. J. L'Heureux, Y. Bengio, K. Burgess, and H. U. Saragovi. Selective small molecule peptidomimetic ligands of TrkC and TrkA receptors afford discrete or complete neurotrophic activities. *Chem Biol*, 12:1015–1028, 2005.

[189] F Fogolari, A Brigo, and H Molinari. The Poisson-Boltzmann equation for biomolecular electrostatics: a tool for structural biology. *J. Mol. Recognit.*, 15:377–392, 2002.

[190] T. Kortemme and D. Baker. A simple physical model for binding energy hot spots in protein-protein complexes. *Proc Natl Acad Sci U S A*, 99:14116–14121, 2002.

[191] T. Kortemme, D. E. Kim, and D. Baker. Computational alanine scanning of protein-protein interfaces. *Sci. STKE*, 2004:pl2, 2004.

[192] J Wang, P Cieplak, and PA Kollman. How well does a restrained electrostatic potential (RESP) model perform in calcluating conformational energies of organic and biological molecules? *J. Comput. Chem.*, 21:1049–1074, 2000.

[193] J W Ponder and D A Case. Force fields for protein simulations. *Adv Protein Chem*, 66:27–85, 2003.

[194] WL Jorgensen, J Chandrasekhar, J Madura, and ML Klein. Comparison of simple potential functions for simulating liquid water. *J. Chem. Phys.*, 79:926–935, 1983.

[195] C I Bayly, P Cieplak, W D Cornell, and P A Kollman. A well-behaved electrostatic potential based method using charge restraints for deriving atomic charges - The RESP model. *J of Phys Chem*, 97(40):10269–10280, 1993.

[196] W D Cornell, P Cieplak, C I Bayly, and P A Kollman. Application of RESP charges to calculate conformational energies, hydrogen-bond energies, and free-energies of solvation. *J of the American Chemical Society*, 115(21):9620–9631, 1993.

[197] E. Lindahl, B. Hess, and D. van der Spoel. Gromacs 3.0: A package for molecular simulation and trajectory analysis. *J. Mol. Mod.*, 7:306–317, 2001.

[198] W F van Gunsteren and H J C A Berendsen. A leap-frog algorithm for stochastic dynamics. *Mol Sim*, 1:173–185, 1988.

[199] B Hess, H Bekker, HJC Berendsen, and JGEM Fraaije. LINCS: A linear constraint solver for molecular simulations. *J of Comp Chem*, 18:1463–1472, 1997.

[200] P Ewald. Die berechnung optischer und elektrostatischer gitterpotentiale. *Ann Phys*, 64:253–287, 1921.

[201] C Sagui and TA Darden. Molecular dynamics simulations of biomolecules: long-range electrostatic effects. *Annu Rev Biophys Biomol Struct*, 28:155–179, 1999.

[202] T Darden, D York, and L Pedersen. Particle mesh Ewald: an Nlog(N) method for Ewald sums in large systems. *J Chem Phys*, 98:10089–10092, 1993.

[203] U Essmann, L Perera, ML Berkowitz, T Darden, H Lee, and LG Pedersen. A smooth particle mesh Ewald method. *J Chem Phys*, 103:8577–8593, 1995.

[204] H J C Berendsen, J P M Postma, A DiNola, and J R Haak. Molecular dynamics with coupling to an external bath. *J. Chem. Phys.*, 81:3684–3690, 1984.

[205] S Nosé and ML Klein. Constant pressure molecular dynamics for molecular systems. *Mol. Phys.*, 50:1055–1076, 1983.

[206] S Nosé. A molecular dynamics method for simulations in the canonical ensemble. *Mol. Phys.*, 52:255–268, 1984.

[207] M Parrinello and A Rahman. Polymorphic transitions in single crystals: a new molecular dynamics approch. *J. Appl. Phys.*, 52:7182–7190, 1981.

[208] D Bashford and D A Case. Generalized Born models of macromolecular solvation effects. *Annu Rev Phys Chem*, 51:129–152, 2000.

[209] Tsui V and Case DA. Theory and applications of the generalized Born solvation model in macromolecular simulations department of molecular biology. *Biopolymers (Nucleic Acid Sciences)*, 56:275–291, 2001.

[210] Still WK, Tempczyk A, Hawley RC, and Hendrickson T. Semianalytical treatment of solvation for molecular mechanics and dynamics. *J. Am. Chem. Soc.*, 112:6127–6129, 1990.

[211] H. Grubmuller, B. Heymann, and P. Tavan. Ligand binding: molecular mechanics calculation of the streptavidin-biotin rupture force. *Science*, 271:997–999, 1996.

[212] B. Isralewitz, S. Izrailev, and K. Schulten. Binding pathway of retinal to bacterio-opsin: a prediction by molecular dynamics simulations. *Biophys J*, 73:2972–2979, 1997.

[213] S. Izrailev, S. Stepaniants, M. Balsera, Y. Oono, and K. Schulten. Molecular dynamics study of unbinding of the avidin-biotin complex. *Biophys J*, 72:1568–1581, 1997.

[214] B. Isralewitz, M. Gao, and K. Schulten. Steered molecular dynamics and mechanical functions of proteins. *Curr Opin Struct Biol*, 11:224–230, 2001.

[215] D. Kosztin, S. Izrailev, and K. Schulten. Unbinding of retinoic acid from its receptor studied by steered molecular dynamics. *Biophys J*, 76:188–197, 1999.

[216] M. V. Bayas, K. Schulten, and D. Leckband. Forced detachment of the CD2-CD58 complex. *Biophys J*, 84:2223–2233, 2003.

[217] S. J. Marrink, O. Berger, P. Tieleman, and F. Jahnig. Adhesion forces of lipids in a phospholipid membrane studied by molecular dynamics simulations. *Biophys J*, 74:931–943, 1998.

[218] H. Grubmuller. Force probe molecular dynamics simulations. *Methods Mol Biol*, 305:493–515, 2005.

[219] A. C. Lorenzo and P. M. Bisch. Analyzing different parameters of steered molecular dynamics for small membrane interacting molecules. *J Mol Graph Model*, 24:59–71, 2005.

[220] B Lee and F M Richards. The interpretation of protein structures: estimation of static accessibility. *J Mol Biol*, 55:379–400, 1971.

[221] F Eisenhaber, P Lijnzaad, P Argos, C Sander, and M Scharf. The double cube lattice method: Efficient approaches to numerical integration of surface area and volume and to dot surface contouring of molecular assemblies. *J. Comp. Chem.*, 16:273–284, 1995.

[222] G Vriend. WHAT IF: a molecular modeling and drug design program. *J Mol Graph*, 8:52–56, 1990.

[223] Sitkoff D, Sharp KA, and Honig B. Accurate calculation of hydration free energies using macroscopic solvent models. *J.Phys.Chem.*, 98:1978–1988, 1994.

[224] R Kazmierkiewicz, C Czaplewski, B Lammek, and J Ciarkowski. Essential dynamics/factor analysis for the interpretation of molecular dynamics trajectories. *J Comput Aided Mol Des*, 13:21–33, 1999.

[225] A Amadei, A B Linssen, and H J Berendsen. Essential dynamics of proteins. *Proteins*, 17:412–425, 1993.

[226] T Ichiye and M Karplus. Collective motions in proteins: a covariance analysis of atomic fluctuations in molecular dynamics and normal mode simulations. *Proteins*, 11:205–217, 1991.

[227] B Hess. Similarities between principal components of protein dynamics and random diffusion. *Phys Rev E*, 62:8438–8448, 2000.

[228] B Hess. Convergence of sampling in protein simulations. *Phys Rev E*, 65:031910, 2002.

[229] A R Atilgan, S R Durell, R L Jernigan, M C Demirel, O Keskin, and Bahar I. Anisotropy of fluctuation dynamics of proteins with an elastic network model. *Biophys J*, 80:505–515, 2001.

[230] I Bahar, A R Atilgan, and B Erman. Direct evaluation of thermal fluctuations in proteins using a single-parameter harmonic potential. *Fold Des*, 2(3):173–181, 1997.

[231] P Doruker, R L Jernigan, and I Bahar. Dynamics of large proteins through hierarchical levels of coarse-grained structures. *J Comput Chem*, 23(1):119–127, 2002.

[232] N A Baker, D Sept, S Joseph, M J Holst, and J A McCammon. Electrostatics of nanosystems: application to microtubules and the ribosome. *Proc Natl Acad Sci U S A*, 98:10037–41, 2001.

[233] W. F. van Gunsteren and M. Karplus. Effect of constraints, solvent and crystal environment on protein dynamics. *Nature*, 293:677–678, 1981.

[234] A J Oakley, K V Loscha, P M Schaeffer, E Liepinsh, G Pintacuda, M C Wilce, G Otting, and N E Dixon. Crystal and solution structures of the helicase-binding domain of escherichia coli primase. *J Biol Chem*, 280:11495–11504, 2005.

[235] W. Humphrey, A. Dalke, and K. Schulten. VMD - Visual Molecular Dynamics. *J Molec Graphics*, 14:33–38, 1996.

[236] M Punta, A Cavalli, V Torre, and P Carloni. Molecular modeling studies on CNG channel from bovine retinal rod: a structural model of the cyclic nucleotide-binding domain. *Proteins*, 52:332–338, 2003.

[237] WG Hoover. Canonical dynamics: equilibrium phase-space distributions. *Phys. Rev. A*, 31:1695–1697, 1985.

[238] H. J. C. Berendsen, D. van der Spoel, and R. van Drunen. GROMACS: A message-passing parallel molecular dynamics implementation. *Comp. Phys. Comm.*, 91:43–56, 1995.

[239] AE Garcia. Large-amplitude nonlinear motions in proteins. *Phys Rev Lett*, 68:2696–2699, 1992.

[240] K A Sharp and B Honig. Electrostatic interactions in macromoleculaes: Theory and applications. *Annu. Rev. Biophys. Biophys. Chem.*, 19:301–332, 1990.

[241] L Laaksonen. A graphics program for the analysis and display of molecular dynamics trajectories. *J Mol Graph*, 10:33–34, 1992.

[242] D L Bergman, L Laaksonen, and A Laaksonen. Visualization of solvation structures in liquid mixtures. *J Mol Graph Model*, 15:301–306, 1997.

[243] R Koradi, M Billeter, and K Wthrich. MOLMOL: a program for display and analysis of macromolecular structures. *J Mol Graphics*, 14:51–55, 1996.

[244] RH Henchman, HL Wang, SM Sine, P Taylor, and JA McCammon. Ligand-induced conformational change in the $\alpha 7$ nicotinic receptor ligand binding domain. *Biophys J*, 88:2564–2576, 2005.

[245] RJ Law, RN Henchman, and JA McCammon. A gating mechanism proposed from a simulation of a human $\alpha 7$ nicotinic acetylcholine receptor. *Proc Natl Acad Sci U S A*, 102:6813–6818, 2005.

[246] S Haider, A Grottesi, BA Hall, FM Ashcroft, and MS Sansom. Conformational dynamics of the ligand-binding domain of inward rectifier K channels as revealed by molecular dynamics simulations: toward an understanding of Kir channel gating. *Biophys J*, 88:3310–3320, 2005.

[247] K Matulef, GE Flynn, and WN Zagotta. Molecular rearrangements in the ligand-binding domain of cyclic nucleotide-gated channels. *Neuron*, 24:443–452, 1999.

[248] D.A. Case, D.A. Pearlman, J.W. Caldwell, T.E. Cheatham III, J. Wang, W.S. Ross, C.L. Simmerling, T.A. Darden, K.M. Merz, R.V. Stanton, A.L. Cheng, J.J. Vincent, M. Crowley, V. Tsui, H. Gohlke, R.J. Radmer, Y. Duan, J. Pitera, I. Massova, G.L. Seibel, U.C. Singh, P.K. Weiner, and P.A. Kollman. Amber 7. University of California, San Francisco, 2002.

[249] T Horiuchi and N Go. Projection of Monte Carlo and molecular dynamics trajectories onto the normal mode axes: human lysozyme. *Proteins*, 10:106–116, 1991.

[250] W Kabsch and C Sander. Dictionary of protein secondary structure: pattern recognition of hydrogen-bonded and geometrical features. *Biopolymers*, 22:2577–2637, 1983.

[251] TM Raschke, J Tsai, and M Levitt. Quantification of the hydrophobic interaction by simulations of the aggregation of small hydrophobic solutes in water. *Proc Natl Acad Sci U S A*, 98:5965–5969, 2001.

[252] M Karplus and GA Petsko. Molecular dynamics simulations in biology. *Nature*, 347:631–639, 1990.

[253] T W Allen, O S Andersen, and B Roux. On the importance of atomic fluctuations, protein flexibility, and solvent in ion permeation. *J Gen Physiol*, 124:679–679, 2004.

[254] K B Craven and W N Zagotta. Salt bridges and gating in the COOH-terminal region of HCN2 and CNGA1 channels. *J Gen Physiol*, 124:663–677, 2004.

[255] X Zong, C Eckert, H Yuan, C Wahl-Schott, H Abicht, L Fang, R Li, P Mistrik, A Gerstner, B Much, L Baumann, S Michalakis, R Zeng, Z Chen, and M Biel. A novel mechanism of modulation of hyperpolarization-activated cyclic nucleotide-gated channels by Src kinase. *J Biol Chem*, 280:34224–34232, 2005.

[256] I Massova and P A Kollman. Computational alanine scanning to probe protein-protein interactions: a novel approch to evaluate binding free energies. *J of American Chemical Society*, 121:8133–8143, 1999.

[257] V Tsui and DA Case. Molecular dynamics simulations of nucleic acids with a generalized Born solvation model. *J. Am. Chem. Soc.*, 122:2489–2498, 2000.

[258] ML Connolly. Solvent-accessible surfaces of proteins and nucleic acids. *Science*, 221:709–713, 1983.

[259] A. Fersht. *Structure and mechanism in protein science: a guide to enzyme catalysis and protein folding*. New York Freeman W.H., 1999.

[260] M H Ultsch, C Wiesmann, L C Simmons, J Henrich, M Yang, D Reilly, S H Bass, and A M de Vos. Crystal structures of the neurotrophin-binding domain of TrkA, TrkB and TrkC. *J Mol Biol*, 290:149–159, 1999.

[261] S. Covaceuszach, A. Cattaneo, and D. Lamba. Neutralization of NGF-TrkA receptor interaction by the novel antagonistic anti-TrkA monoclonal antibody MNAC13: A structural insight. *Proteins*, 58:717–727, 2005.